

**AFRL-SN-RS-TR-2005-365, Volume 2 (of 2)**  
**Final Technical Report**  
**October 2005**



**PARALLEL SCENE  
GENERATION/ELECTROMAGNETIC MODELING  
OF COMPLEX TARGETS IN COMPLEX CLUTTER  
AND PROPAGATION ENVIRONMENTS**

**Black River Systems Company**

*APPROVED FOR PUBLIC RELEASE; DISTRIBUTION UNLIMITED.*

**AIR FORCE RESEARCH LABORATORY  
SENSORS DIRECTORATE  
ROME RESEARCH SITE  
ROME, NEW YORK**

## **STINFO FINAL REPORT**

This report has been reviewed by the Air Force Research Laboratory, Information Directorate, Public Affairs Office (IFOIPA) and is releasable to the National Technical Information Service (NTIS). At NTIS it will be releasable to the general public, including foreign nations.

AFRL-SN-RS-TR-2005-365, Volume 2 (of 2), has been reviewed and is approved for publication

APPROVED:

/s/  
CARL R. THOMAS  
Project Engineer

FOR THE DIRECTOR:

/s/  
RICHARD G. SHAUGHNESSY, Chief  
Rome Operations Office  
Sensors Directorate

REPORT DOCUMENTATION PAGE			Form Approved OMB No. 074-0188	
Public reporting burden for this collection of information is estimated to average 1 hour per response, including the time for reviewing instructions, searching existing data sources, gathering and maintaining the data needed, and completing and reviewing this collection of information. Send comments regarding this burden estimate or any other aspect of this collection of information, including suggestions for reducing this burden to Washington Headquarters Services, Directorate for Information Operations and Reports, 1215 Jefferson Davis Highway, Suite 1204, Arlington, VA 22202-4302, and to the Office of Management and Budget, Paperwork Reduction Project (0704-0188), Washington, DC 20503				
1. AGENCY USE ONLY (Leave blank)		2. REPORT DATE OCTOBER 2005		3. REPORT TYPE AND DATES COVERED Final Sep 01 – Sep 04
4. TITLE AND SUBTITLE PARALLEL SCENE GENERATION/ELECTROMAGNETIC MODELING OF COMPLEX TARGETS IN COMPLEX CLUTTER AND PROPAGATION ENVIRONMENTS			5. FUNDING NUMBERS C - F30602-01-C-0203 PE - 62204F PR - HPCM TA - 00 WU - 02	
6. AUTHOR(S) Milissa Benincasa, Tapan Sarkar, Christopher Card, Carl Thomas, Eric Mokole, Douglas Taylor, Richard Schneible, Ravi Adve, Michael Simcoe, Laurie Joiner				
7. PERFORMING ORGANIZATION NAME(S) AND ADDRESS(ES)  Black River Systems Company 162 Genesee Street Utica NY 13502			8. PERFORMING ORGANIZATION REPORT NUMBER  N/A	
9. SPONSORING / MONITORING AGENCY NAME(S) AND ADDRESS(ES)  AEDC/DOT 1099 Avenue C Arnold AFB TN 37389-9011			10. SPONSORING / MONITORING AGENCY REPORT NUMBER  AFRL-SN-RS-TR-2005-365 Volume 2 (of 2)	
11. SUPPLEMENTARY NOTES AFRL Project Engineer: Carl R. Thomas/SNRT/(315) 330-2600 AEDC Portfolio Leader: Jere Matty/DOT/(931) 454-6515			<a href="mailto:Carl.Thomas@rl.af.mil">Carl.Thomas@rl.af.mil</a> <a href="mailto:Jere.Matty@arnold.af.mil">Jere.Matty@arnold.af.mil</a>	
12a. DISTRIBUTION / AVAILABILITY STATEMENT  APPROVED FOR PUBLIC RELEASE; DISTRIBUTION UNLIMITED.				12b. DISTRIBUTION CODE
13. ABSTRACT (Maximum 200 Words) Under the Department of Defense (DoD) Common High Performance Computing Software Support Initiative (CHSSI), the goal of this effort was to parallelize the electromagnetic modeling tool WIPL-D (Wires, Plates and Dielectrics). WIPL-D utilizes a Method of Moments technique to solve Maxwell's Equations. Three evaluation criteria were used to evaluate the effort: 1) accuracy of the code as compared to the commercial program WIPL-D; 2) scalability of the code when using multi-processor High Performance Computing (HPC) resources; and 3) portability of the code, by running on multiple HPC computers with different computing architectures. A demonstration of a cell phone beside a head was used to demonstrate the codes utility and performance.				
14. SUBJECT TERMS High Performance Computing, Parallel Processing, Radar Scene Generation, Electromagnetic Modeling, Method of Moments				15. NUMBER OF PAGES 45
				16. PRICE CODE
17. SECURITY CLASSIFICATION OF REPORT  UNCLASSIFIED	18. SECURITY CLASSIFICATION OF THIS PAGE  UNCLASSIFIED	19. SECURITY CLASSIFICATION OF ABSTRACT  UNCLASSIFIED	20. LIMITATION OF ABSTRACT  UL	

## TABLE OF CONTENTS

<b>RESULTS SUMMARY .....</b>	<b>IV</b>
<b>EXECUTIVE SUMMARY.....</b>	<b>1</b>
<b>1.0 INTRODUCTION.....</b>	<b>2</b>
<b>2.0 SYNTHETIC APERTURE RADAR (SAR) .....</b>	<b>3</b>
2.1. SAR GEOMETRY .....	3
2.2. SAR PARAMETERS .....	4
<b>3.0 SIMULATING SAR DATA USING WIPL-D.....</b>	<b>6</b>
3.1. THE WIPL-D MODEL.....	7
3.2. TIMING ISSUES IN THE WIPL-D SIMULATIONS .....	8
<b>4.0 METAL TARGET EXAMPLES.....</b>	<b>10</b>
4.1. BASIC METAL TARGETS.....	10
4.1.1. <i>Two plates</i> .....	10
4.1.2. <i>Three plates</i> .....	12
4.1.3. <i>Plates with ridges</i> .....	14
4.2. ADVANCED METAL TARGETS .....	16
4.2.1. <i>Single T80 tank</i> .....	16
4.2.2. <i>Twin broadside T80 tanks</i> .....	19
4.2.3. <i>Twin rotated T80 tanks</i> .....	19
<b>5.0 TARGET EXAMPLES INVOLVING FOLIAGE.....</b>	<b>21</b>
5.1. A SIMPLE TREE MODEL .....	22
5.2. A SCENE WITH DIELECTRIC AND BASIC METAL TARGETS: TRIHEDRAL CORNER REFLECTOR AND DIELECTRIC TREE.....	25
5.3. A SCENE WITH DIELECTRIC AND METAL TARGETS: T80 TANK AND SIMPLE TREE MODEL ..	27
5.4. A PRACTICAL FOPEN SCENE .....	29
<b>6.0 LINEAR SUPERPOSITION APPROACH.....</b>	<b>31</b>
<b>7.0 SCENES WITH MOVING TARGETS .....</b>	<b>33</b>
<b>8.0 RECOMMENDED WIPL-D MODIFICATIONS .....</b>	<b>35</b>
<b>9.0 REVIEW .....</b>	<b>36</b>
<b>10.0 REFERENCES.....</b>	<b>37</b>

## List of Figures

Figure 1: Synthetic aperture radar geometry; (a) Three-dimensional (physical) geometry; (b) Reduced two-dimensional (simplified) geometry. ....	3
Figure 2: A typical transmit pulse $p(t)$ .....	5
Figure 3: The corresponding frequency domain transmit pulse spectrum $P(f)$ .....	6
Figure 4: A typical plot of the frequency response $W(f)$ for a target scene .....	7
Figure 5: (a) Two-plate WIPL geometry; (b) $E_{\varphi\varphi}$ backprojection spotlight SAR reconstruction. ....	11
Figure 6: (a) Two-plate WIPL geometry; (b) $E_{\theta\theta}$ backprojection spotlight SAR reconstruction.....	11
Figure 7: (a) Three-plate WIPL geometry; (b) $E_{\varphi\varphi}$ backprojection spotlight SAR reconstruction...	13
Figure 8: (a) Three-plate WIPL geometry; (b) $E_{\theta\theta}$ backprojection spotlight SAR reconstruction...	13
Figure 9: Ridged plate WIPL geometry. (a) Large ridges; (b) small ridges.....	14
Figure 10: (a) Large ridge plate WIPL geometry; (b) $E_{\varphi\varphi}$ backprojection spotlight SAR reconstruction .....	15
Figure 11: (a) Small ridge plate WIPL geometry; (b) $E_{\varphi\varphi}$ backprojection spotlight SAR reconstruction .....	16
Figure 12: T80 tank WIPL geometry .....	17
Figure 13: (a) T80 tank WIPL geometry; (b) $E_{\varphi\varphi}$ backprojection spotlight SAR reconstruction .....	18
Figure 14: (a) T80 tank WIPL geometry; (b) $E_{\theta\theta}$ backprojection spotlight SAR reconstruction .....	19
Figure 15: (a) Broadside twin T80 tank WIPL geometry; (b) backprojection spotlight SAR reconstruction. ....	20
Figure 16: (a) Rotated twin T80 WIPL geometry; (b) backprojection spotlight SAR reconstruction .....	20
Figure 17: Time-domain SAR signal after matched filtering. (a) Broadside twin T80 simulation; (b) rotated twin T80 simulation .....	21
Figure 18: A dielectric tree target .....	22
Figure 19: Tree dimensions and permittivity assignments .....	23
Figure 20: (a) Dielectric tree WIPL geometry; (b) backprojection spotlight SAR reconstruction ...	23
Figure 21: Time-domain SAR signal for the dielectric tree after matched filtering.....	24
Figure 22: Trihedral corner reflector and dielectric tree WIPL geometry .....	25
Figure 23: Trihedral corner reflector $E_{\varphi\varphi}$ backprojection spotlight SAR reconstruction.....	26
Figure 24: Trihedral corner and dielectric tree $E_{\varphi\varphi}$ backprojection spotlight SAR reconstruction..	26
Figure 25: T80 tank and dielectric tree geometry .....	27
Figure 26: (a) T80 tank WIPL geometry; (b) backprojection spotlight SAR reconstruction.....	28
Figure 27: (a) T80 tank and dielectric tree WIPL geometry; (b) backprojection spotlight SAR reconstruction. Compare with Figure 20b and Figure 26b. ....	28
Figure 28: A practical FOPEN scene featuring a tank with dielectric trees and ground plane. ....	30
Figure 29: Practical FOPEN scene backprojection spotlight SAR $E_{\varphi\varphi}$ reconstruction.....	30
Figure 30: Twin T80 backprojection spotlight SAR $E_{\varphi\varphi}$ reconstruction. (a) Simulating both T80 tanks in the same scene; (b) Using superposition from a single T80 simulation. ....	32
Figure 31: T80 tank and dielectric tree sparse forest WIPL geometry.....	32

<b>Figure 32: (a) T80 tank and dielectric tree sparse forest WIPL geometry; (b) backprojection spotlight SAR reconstruction using superposition .....</b>	<b>33</b>
<b>Figure 33: Basic moving target example with a stationary and moving trihedral corner reflector..</b>	<b>34</b>
<b>Figure 34: Backprojection spotlight SAR reconstruction. (a) <math>v=1.5\text{km/h}</math>; (b) <math>v=5.0\text{km/h}</math>; (c) <math>v=29.7\text{km/h}</math>.....</b>	<b>35</b>

### List of Tables

<b>Table 1: SAR dimensions .....</b>	<b>10</b>
<b>Table 2: T80 tank dimensions .....</b>	<b>17</b>
<b>Table 3: Moving target simulation parameter values.....</b>	<b>34</b>

## Results Summary

*(Results in bold are of particular interest)*

### *Metal targets:*

Figure Page #	Target	Description	BW (MHz)	Freq. range (MHz)	Unknowns @ $f_{\max}$
Figure 5 Page 11	Two metal plates	Three-meter square and circular plates for $E_{\varphi\varphi}$ polarization	400	100-500	1080
Figure 6 Page 11	Two metal plates	Three-meter square and circular plates for $E_{\theta\theta}$ polarization	400	100-500	1080
Figure 7 Page 13	Three metal plates	Three-meter square, circular and rotated square plates for $E_{\varphi\varphi}$ polarization	400	100-500	1692
Figure 8 Page 13	Three metal plates	Three-meter square, circular and rotated square plates for $E_{\theta\theta}$ polarization	400	100-500	1692
Figure 10 Page 15	Large ridged plate	Three-meter square plate with large triangular ridges added to emulate surface roughness	400	100-500	1190
Figure 11 Page 16	Small ridged plate	Three-meter square plate with small triangular ridges added to emulate surface roughness	400	100-500	1838
<b>Figure 13 Page 18</b>	<b>T80 tank</b>	<b>Single broadside oriented T80 tank for <math>E_{\varphi\varphi}</math> polarization</b>	<b>250</b>	<b>100-350</b>	<b>2943</b>
<b>Figure 14 Page 19</b>	<b>T80 tank</b>	<b>Single broadside oriented T80 tank for <math>E_{\theta\theta}</math> polarization</b>	<b>250</b>	<b>100-350</b>	<b>2943</b>
<b>Figure 15 Page 20</b>	<b>Twin broadside T80 tanks</b>	<b>Twin T80 tanks; one at the center of the STR and the other displaced</b>	<b>230</b>	<b>100-330</b>	<b>5388</b>
<b>Figure 16 Page 20</b>	<b>Twin rotated T80 tanks</b>	<b>Twin T80 tanks; one at the center of the STR and the other displaced and rotated</b>	<b>230</b>	<b>100-330</b>	<b>5388</b>

*Dielectric targets:*

Figure	Target	Description	BW (MHz)	Freq. range (MHz)	Unknowns @ $f_{\max}$
Figure 20 Page 23	Dielectric tree	Dielectric tree; the branch body has $\varepsilon_r = 6$ and the trunk has $\varepsilon_r = 7$ .	230	100-330	3416
Figure 27 Page 28	Dielectric tree and T80 tank	The T80 tank signature obscured by the dielectric tree	230	100-330	7445
Figure 29 Page 30	T80 tank, foliage and ground plane	Practical FOPEN scene	84	40-124	9995
Figure 32 Page 33	T80 tank and dielectric tree sparse forest	T80 tank and dielectric tree sparse forest reconstruction obtained using superposition.	230	100-330	N/A
Figure 34 Page 35	Basic moving target	Stationary and moving trihedral corner reflectors	200	100-300	1234

## Executive Summary

Within the larger project of developing a parallel version of WIPL-D (WIPL-DP), this sub-project deals with investigating applications of interest to the Air Force. In this regard, the focus thus far has been mainly on developing the capability to model foliage penetrating (FOPEN) synthetic aperture radar (SAR) scenes. The goal of this effort is to be able to generate *realistic* FOPEN SAR simulations.

This study describes the use of WIPL-D to model SAR scenes and moving airborne platforms. The frequency domain data obtained by the analysis is transformed via a Fourier transform to the time domain. This time domain data is then used to generate SAR images of the radar scene.

A crucial contributor to the success of this effort has been the use of the capabilities within WIPL-D to model incoming plane waves as phase shifts between objects even in the far field option. Another crucial feature used is the reduced current expansion option that results in good image quality in significantly reduced execution time. Even with this reduction, however, the basic FOPEN result shown in Figure 27 of a single T80 tank and basic tree model took over three weeks to complete on a single processor. In this regard, we believe that the result shown in Figure 27 extends the capabilities of the current single processor version WIPL-D to their limit. The advanced FOPEN scene shown in Figure 28 featuring realistic foliage and ground effects absolutely requires the parallel version to WIPL-D (WIPL-DP) to analyze over any practical frequency range. The maximum number of unknowns for the single processor version (10,000) has been reached.

The scattered field frequency domain output data from WIPL-D is used to form SAR images of a target scene. Results are given for basic metal targets (plates), complex metal targets (tanks), and basic scenes involving dielectric and metal targets. These results demonstrate that targets appear at the correct location and with the approximate correct dimension and shape. After confirming WIPL-D's capacity to analyze SAR scenes, a couple of practical FOPEN scenes are shown. Due to the inherent size limitations in the single processor version, these scenes are only shown over a limited frequency range. However, these results can be easily extended over a more realistic frequency range once the parallel version becomes available. The parallel version will make the ability to generate realistic SAR scenes with WIPL-DP a reality using the framework built in this study.

## 1.0 Introduction

This project will develop a scalable, portable, parallel scene generation (PSG) tool that will provide tri-service capability to quickly/rapidly generate scenes of radiating and scattering structures (targets and their surrounding environment) in realistically complex electromagnetic environments. This improvement will move users from accurate modeling of targets only to accurate modeling of targets in their environment. This PSG tool will be applicable to a wide range of end-user applications in the Army, Navy, Air Force and Marines. Example DoD missions that benefit from such a tool include:

- Detection of Targets under Trees
- Ship Radar Performance
- Strategic Subsurface Target Detection
- Land Mine Imaging
- Ballistic Missile Discrimination

The scene generation tool requires an electromagnetic analysis engine to model the interaction between target and surrounding dielectric regions. The program used for this purpose is called WIPL-D (Wires, Plates and Dielectrics). WIPL-D was specifically chosen over other software for several key reasons. It combines the excellent accuracy inherent in a method of moments (MOM) approach with the high efficiency of entire domain basis functions (10-20 unknowns per square wavelength). WIPL-D is the only commercially available electromagnetics analysis software tool capable of efficiently analyzing electromagnetic radiation and scattering in electrically large scenes with both metal and complex, lossy, dielectrics. A parallel version of WIPL-D (WIPL-DP) is currently being developed to solve extremely large matrix equations in order to enable the accurate analysis of very large scenes of interest such as targets under foliage (FOPEN) and buried targets (strategic subsurface target detection). This tool will permit transition from accurate modeling of complex targets (today's capability) to accurate modeling of complex targets in complex environments with all their associated scattering and propagation effects.

WIPL-DP will be able to accurately model complex interactions between objects illuminated by the transmitter including non-homogeneous foliage/ground layers. In important applications such as foliage penetration (FOPEN) radar or subsurface target detection, the interference to the signal is the complex propagation through the target's environment. The ability to isolate a desired signal from this interference is needed. WIPL-D inherently has the capability to model the propagation through foliage/ground layers and the complex interactions between non-homogeneous material bodies. However, WIPL-D does not have the innate ability to model all possible types of scenes. The signals to be simulated must be generated using the scattered frequency domain output electric and magnetic field. Using the frequency domain output fields to simulate SAR FOPEN scenes is the topic of this study. Example results are shown for basic scenes to confirm the operation followed by scenes with FOPEN type characteristics.

## 2.0 Synthetic Aperture Radar (SAR)

Synthetic aperture radar (SAR) is an imaging system that uses the motion of a radar carrying vehicle or the motion of a radar target to extract information. This information is usually used to generate an image of a specific target or target scene with resolution corresponding to the entire synthetic aperture. This report is concerned with spotlight mode synthetic aperture radar, a particular form of SAR. We begin with a review of the operation of spotlight mode SAR. This review, based upon the description provided in [5], also serves to introduce the notation used in this report.

### 2.1. SAR Geometry

The general spotlight mode synthetic aperture radar (SAR) geometry is shown in Figure 1a. The box shown centered at the origin is the spotlighted target region (STR). It has dimensions of  $2X_o$  and  $2Y_o$  in the  $x$ - and  $y$ - direction respectively. The synthetic aperture that corresponds to the aircraft flight path is symmetrical about the STR and has a total length of  $2L$ . The synthetic aperture is located at an elevation  $Z$  and at a distance  $X'$  in the  $x'$ -direction away from the center of the STR.

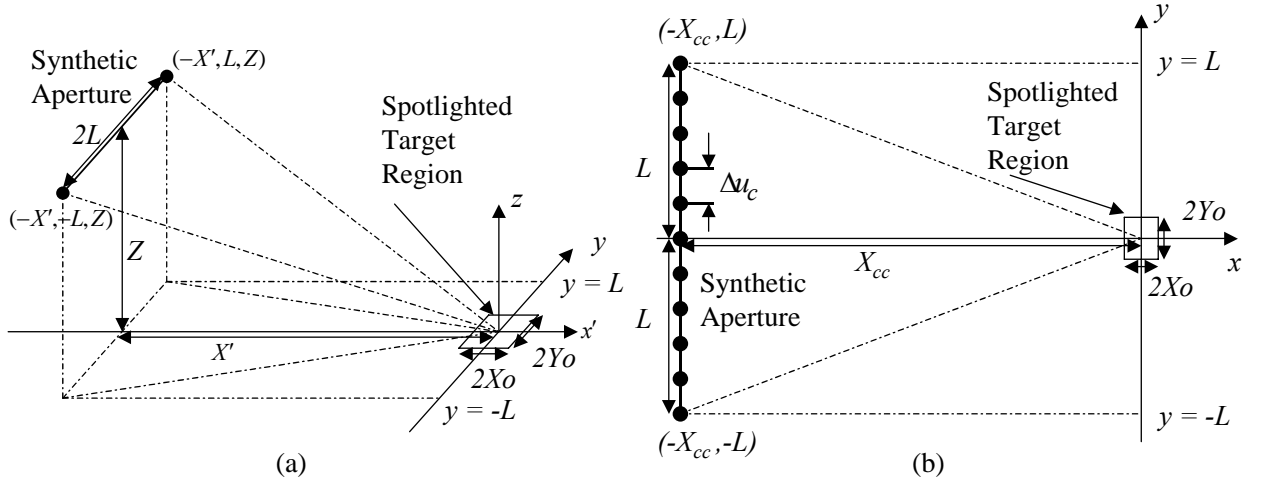


**Figure 1: Synthetic aperture radar geometry; (a) Three-dimensional (physical) geometry; (b) Reduced two-dimensional (simplified) geometry.**

As the aircraft flies along the synthetic aperture flight path, it sends radar pulses into the STR at regularly spaced intervals and collects the reflected pulses from objects located in the scene. The aircraft antenna array is steered (electronically or mechanically) to always point at the STR. The parameters of the radar pulse specify a frequency range between some minimum frequency point  $f_{\min}$  and maximum frequency point  $f_{\max}$ . The data collected from the reflected pulses along the synthetic aperture can then be used to form an image giving information about the location and geometry of targets within the STR.

Since the distance (and hence the phase shift) in the  $x'$ - and  $z$ - direction to the center of the STR are fixed, the parameters  $X'$  and  $Z$  can be combined into a total distance

$$X_{cc} = \sqrt{(X'^2 + Z^2)}, \quad (1)$$

and corresponding cumulative phase shift to the center of the STR. This term is the slant range to the center of the target region. Combining these parameters eliminates one of the variables producing the reduced geometry shown in Figure 1b, to simplify the subsequent processing. Similarly, in the subsequent analysis discussion, the range variable  $x$  refers to the combined variable  $x = \sqrt{(x'^2 + Z^2)}$ .

## 2.2. SAR Parameters

The resolution is a measure of the ability to distinguish between two closely spaced point scatterers in an image. For the SAR operation described, the  $x$ - and  $y$ - direction resolution is given approximately by

$$\Delta x \cong \frac{c}{4f_o}, \quad (2)$$

$$\Delta y \cong \frac{X_{cc} \lambda_{\max}}{4L}, \quad (3)$$

where  $c$  is the speed of light,  $f_o = (f_{\max} - f_{\min})$  is the pulse bandwidth, and  $\lambda_{\max}$  is the wavelength at the lowest frequency point of the pulse bandwidth. Given these relations, the resolution can be improved by

- increasing the bandwidth
- increasing the aperture length
- decreasing  $\lambda_{\max}$  by increasing the lowest frequency point  $f_{\min}$  of the pulse bandwidth.

However, significantly increasing the lowest frequency point may not be an option since for some of the applications such as foliage penetrating radar (FOPEN) and subsurface target detection it is the lower frequency ranges (VHF and UHF) that are of interest due to their ability to better penetrate foliage and soil. Higher frequency SAR imaging systems with larger fractional bandwidths (for example systems operating near X-band [7]) can achieve very fine resolution but cannot penetrate foliage or soil effectively.

The radar pulses are transmitted at regular intervals with the pulse repetition frequency (PRF). The spacing between these intervals is denoted by  $\Delta u_c$  that is the distance the aircraft travels along the synthetic aperture between pulse transmissions. The PRF must satisfy

$$\Delta u_c \leq \frac{X_{cc} \lambda_{\min}}{4Y_o}, \quad (4)$$

where  $\lambda_{\min}$  is the wavelength at the highest pulse frequency point.

In practice, a linear FM pulse is often used to transmit a broadband pulse. The linear FM pulse, which has a large time bandwidth product, is given by

$$p(t) = \exp[j(\beta t + \alpha t^2)] \quad 0 \leq t \leq T_p \quad (5)$$

where  $T_p$  is the pulse width over which the frequency bandwidth is swept. The parameters  $\alpha$  and  $\beta$  are determined according to the required pulse bandwidth as

$$\alpha = \frac{\pi(f_{\max} - f_{\min})}{T_p} = \frac{\pi f_0}{T_p} \quad (6)$$

$$\beta = 2\pi f_{\min} \quad (7)$$

A plot of a typical FM pulse  $p(t)$  and the corresponding frequency domain spectrum  $P(f)$  is shown in Figure 2 and Figure 3 respectively. The pulse width  $T_p$  is 0.5 $\mu$ sec and the parameters  $\alpha$  and  $\beta$  were chosen to provide a bandwidth of 250MHz between 100MHz-350MHz.

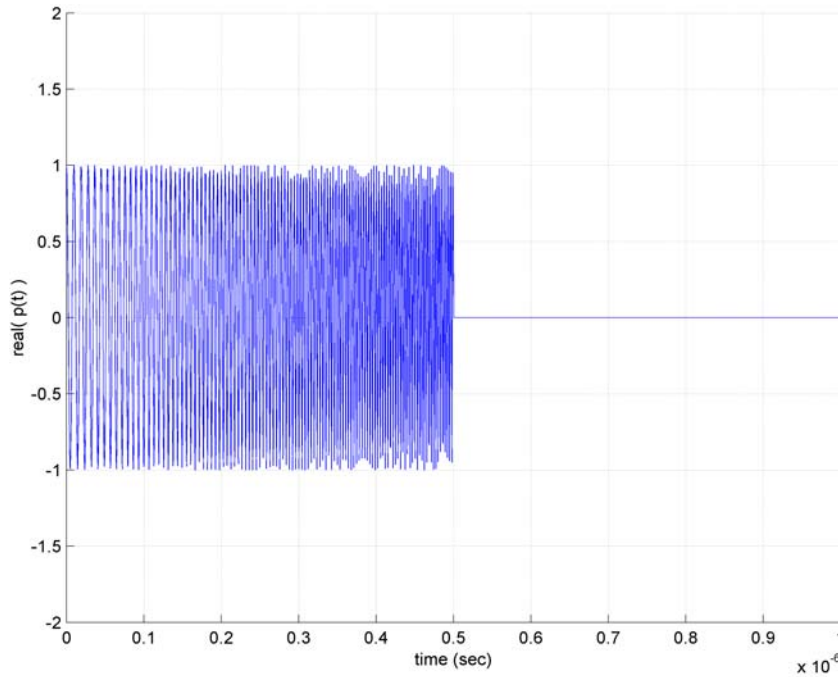


**Figure 2: A typical transmit pulse  $p(t)$**

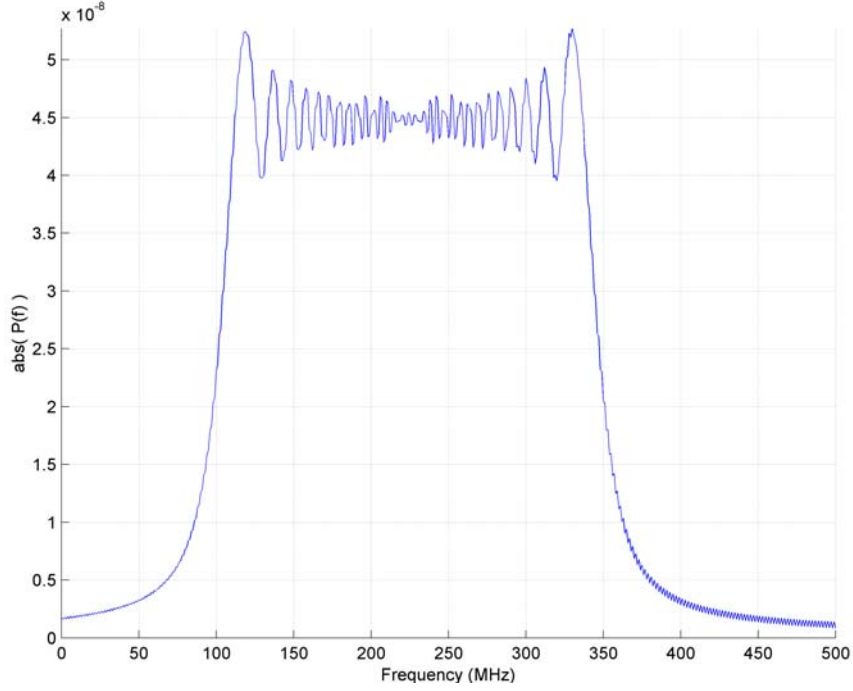


**Figure 3: The corresponding frequency domain transmit pulse spectrum  $P(f)$**

### 3.0 Simulating SAR data using WIPL-D

As with all Method of Moments (MOM) software, WIPL-D analyzes stationary scenes in the frequency domain. However, SAR is a time-domain operation for a changing scene with a moving aircraft. To bridge these two domains, the excitation transmit pulse spectrum  $P(f)$  (see for example Figure 3) is multiplied with the frequency response for the scene at each aperture point along the synthetic aperture. Let  $s(t)$  denote the received time domain signal at a particular aperture point and  $S(f)$  the corresponding frequency domain signal. Also let  $W(f)$  denote the frequency response of the scene, obtained using WIPL-D, at that same aperture point. Then, for that particular aperture point the received signal is given by

$$S(f) = P(f)W(f) \quad (8)$$

The resulting time-domain signal,  $s(t)$ , at that aperture point is given by the inverse Fourier transform of  $S(f)$ . The approach used here may be thought of in terms of a linear system. The frequency response obtained from WIPL-D acts as the impulse response of the system. The transmitted pulse acts as the input to the system and the received signal is output. Therefore the following relation holds

$$s(t) = p(t) * w(t) \xrightarrow{F} S(f) = P(f)W(f) \quad (9)$$

A plot of a typical WIPL-D frequency response  $W(f)$  is given in Figure 4. The simulated frequency range covers a bandwidth of 250MHz from 100MHz-350MHz (specifically, for the center aperture point located at  $y = 0$  for the T80 tank example discussed later in the advanced metal targets section).

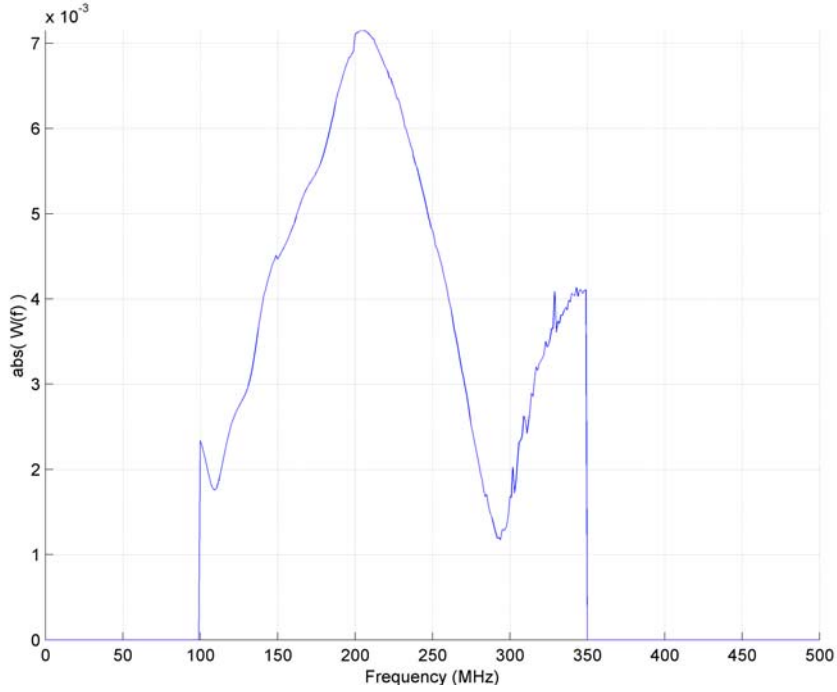


**Figure 4: A typical plot of the frequency response  $W(f)$  for a target scene**

### 3.1. The WIPL-D model

For each frequency point,  $f_i$ , in the pulse bandwidth covered, a WIPL-D simulation of the target scene is performed to extract the frequency response. For each aperture point  $(X', y, Z)$  where  $y \in [-L, L]$ , which corresponds to a particular  $(r, \varphi, \theta)$ , a plane wave excitation from that aperture point direction is calculated. A plane wave type excitation is valid since the synthetic aperture is in the STR far-field. In terms of the WIPL-D interface, a monostatic excitation is performed from that aperture point direction. The normalized electric far-field  $e(\varphi, \theta)$  is obtained for that  $(\varphi, \theta)$  aperture point direction. To obtain the magnitude and phase of the electric field at a particular  $r$  position along that  $(\varphi, \theta)$  direction (i.e., for that particular aperture point  $(r, \varphi, \theta)$ ), the normalized electric far-field is moved to that  $r$  radius as

$$E(r, \varphi, \theta) = e(\varphi, \theta) \frac{e^{-jkr}}{r}, \quad (10)$$

where  $k = 2\pi f / c = 2\pi / \lambda$ . Additionally, since in WIPL-D the phase of the incident excitation plane wave for a particular direction is normalized with respect to the origin ( $r=0$ ), the phase shift (lag) of the incident excitation plane wave to the STR must also be included by

$$E'(r, \varphi, \theta) = E(r, \varphi, \theta) \frac{e^{-jkr}}{r} \quad (11)$$

This  $E'(r, \varphi, \theta)$  acts as the  $W(f)$  at the particular aperture point for each particular frequency  $f_i$ .

### 3.2. Timing Issues in the WIPL-D Simulations

The plot of the WIPL-D spectrum  $W(f)$  shown in Figure 4 was obtained by performing simulations at a frequency spacing of  $\Delta f = 1\text{MHz}$  over a 250MHz bandwidth from 100MHz-350MHz. This frequency spacing  $\Delta f$  is important since the total time window that can be supported following the inverse discrete Fourier transform (IDFT) is

$$T_{wind} = 1 / \Delta f \quad (12)$$

For example, with a frequency spacing of  $\Delta f = 1\text{MHz}$  the total time window is  $T_{wind} = 1\mu\text{sec}$ . All of the reflected pulses from the STR must fall within a single time window. This dictates the dimensions  $X_0$  and  $Y_0$  for the STR as well as the synthetic aperture length  $L$  that can be supported. Specifically, the minimum distance from the synthetic aperture to a point in the STR is given by

$$R_{min} = (X_{cc} - X_o) \quad (13)$$

which is the distance from the closest point of approach (CPA), located at  $y = 0$  on the synthetic aperture, to the closest edge of the STR. The maximum distance from the synthetic aperture to a point in the STR is given by

$$R_{max} = \sqrt{((X_{cc} + X_o)^2 + (Y_o + L)^2)} \quad (14)$$

which is the distance from an end point, located at  $y = \pm L$  on the synthetic aperture, to the furthest corner of the STR.

The minimum and maximum times for pulses to return from the STR are:

$$T_{min} = \frac{2R_{min}}{c} \quad (15)$$

$$T_{max} = \frac{2R_{max}}{c} + T_p \quad (16)$$

In words,  $T_{min}$  is the time it would take the leading edge of the pulse to return from a point scatterer located at the minimum distance back to the synthetic aperture;  $T_{max}$  is the time it would take the trailing edge of the pulse to return from a point scatterer located at the maximum distance back to the synthetic aperture. Hence,

$$(T_{max} - T_{min}) \leq T_{wind} \quad (17)$$

$$\frac{2}{c}(R_{max} - R_{min}) \leq T_{wind} - T_p \quad (18)$$

For example, if the time window is  $T_{wind} = 1\mu\text{sec}$  with a pulse width of  $T_p = 0.5\mu\text{sec}$ , then  $(R_{max} - R_{min}) = 75\text{m}$ . The synthetic aperture dimensions of  $X' = 500\text{m}$  and  $Z = 500\text{m}$  and an STR with a length and width of 40 meters ( $X_0 = 20\text{m}$  and  $Y_0 = 20\text{m}$ ) will allow for a synthetic aperture size of  $L = 182\text{m}$ .

A final issue in terms of positioning of the time window will now be detailed. The targets within the STR may be considered to be composed of individual point source scatterers. Let the STR be composed

of  $N$  individual point sources, each with a certain reflectivity magnitude  $\sigma_n$  and time delay  $t_n$  back to the synthetic aperture. The total received signal at a particular synthetic aperture point is then given by the summation (superposition) of the reflected waves from these individual point sources as

$$s(t) = \sum_{n=1}^N \sigma_n p(t - t_n), \quad (19)$$

$$S(f) = \sum_{n=1}^N \sigma_n P(f) e^{-j2\pi f t_n}, \quad (20)$$

$$t_n = \frac{2r_n}{c}, \quad (21)$$

where  $r_n$  is the distance from the particular synthetic aperture point to the  $n^{th}$  point source reflector. When the inverse discrete Fourier transform is performed on the received signal spectrum  $S(f)$  in eqn. (20), the received signal  $s(t)$  will fall within a complete time window  $T_{wind}$  as long as the relation of eqn (17) is satisfied for a given  $\Delta f$  frequency spacing. However, due to the repetition inherent in the discrete Fourier transform (DFT), a portion of the received signal  $s(t)$  may wrap around the end of the time window and appear at the beginning of the time window making partitioning of the  $s(t)$  data difficult.

To circumvent this timing ambiguity, the received signal  $s(t)$  is manipulated to ensure that it appears sequentially in its entirety within a complete time window. To accomplish this, redefine the timing index with respect to the earliest possible time a reflected pulse could return to the synthetic aperture by

$$t_n = T_{min} + t_m \quad (22)$$

$$0 \leq t_m \leq T_{max} \quad (23)$$

Also, let  $\sigma_m = \sigma_n$  since there is no change in the reflectivity magnitude of the individual point source scatterers, but only in their timing index. Then, the received signal can be rewritten as

$$s(t) = \sum_{m=1}^N \sigma_m p[t - (T_{min} + t_m)] \quad (24)$$

$$S(f) = \sum_{m=1}^N \sigma_m P(f) e^{-j2\pi f t_m} e^{-j2\pi f T_{min}} \quad (25)$$

Hence, the fixed phase lag (fixed time delay) up to the beginning of the target box can be temporarily removed by multiplying the  $S(f)$  spectrum as

$$S'(f) = S(f) e^{+j2\pi f T_{min}} \quad (26)$$

before performing the inverse discrete Fourier transform. The fixed time delay  $T_{min}$  that was artificially removed can then be reintroduced by adding it back to the time index of  $s(t)$ . The backprojection spotlight SAR reconstruction algorithm available in [5] is then applied to this received signal  $s(t)$ .

#### 4.0 Metal target examples

This section gives the results for SAR images of an STR consisting only of metal targets. The SAR dimensions are provided in Table 1. These SAR dimensions correspond to a  $\pm 20^\circ$  angular range in  $\varphi$  about the STR. The STR is seen from approximately a  $\theta = 45^\circ$  angle. The  $X'$  and  $Z$  values were chosen to match the allowable STR size given a certain  $T_{min}$  and  $T_{max}$  with  $\Delta f = 1\text{MHz}$  for these examples. Simulations with the incident and received field both polarized along  $\phi$  or  $\theta$  are denoted  $E_{\phi\phi}$  and  $E_{\theta\theta}$  respectively. Changing the frequency spacing or pulse width can accommodate other SAR dimensions.

Dimension	Size (meters)
$X'$	500
$Z$	500
$X_\theta$	20
$Y_\theta$	20
$X_{cc}$	707.1
$L$	182

**Table 1: SAR dimensions**

#### 4.1. Basic metal targets

##### 4.1.1. Two plates

Consider first the target scene shown in Figure 5a. The WIPL geometry shown consists of a three meter square plate at the center of the target region and a circular plate with a three meter diameter which is displaced from the center of the target region a distance of  $(\Delta x, \Delta y) = (-12, 12)$  meters. The plates reside in the  $z = 0$  plane. The pulse bandwidth is 400MHz between 100MHz-500MHz. Figure 5b and Figure 6b show the resulting backprojection spotlight SAR reconstructions. In Figure 5b the transmitted and received field is polarized along  $\varphi$  and in Figure 6b the transmitted and received field is polarized along  $\theta$ . In Figure 5b, the leading edges of both plates are seen and appear at the correct location. The range distance to the edges of the square and circular plates can be calculated as

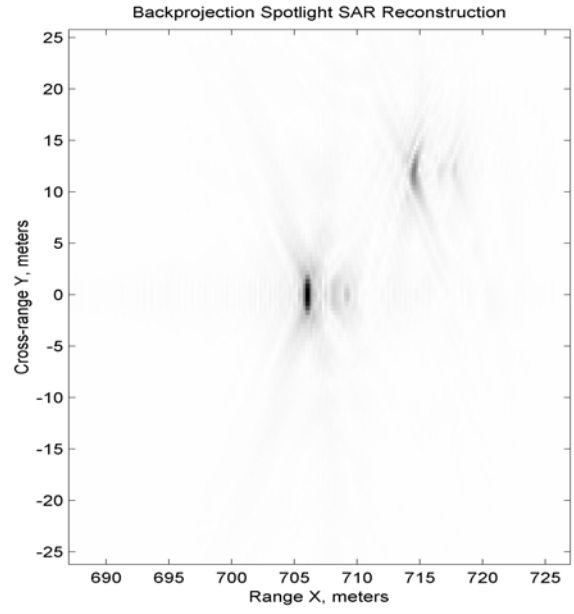
$$X_{sqr} = \sqrt{((500 - 1.5)^2 + (500)^2)} = 706.1m \quad (27)$$

$$X_{circ} = \sqrt{((500 + 12 - 1.5)^2 + (500)^2)} = 714.6m \quad (28)$$

The shape of the target edges (flat edge for the square plate and curved edge for the circular plate) can be seen and the approximate cross-range dimensions of both plates (about three meters) are correct. In Figure 6b, the trailing edge of the square plate can be seen and a portion of the circular plate near the trailing edge also appears. An explanation for the appearance of this edge is that the  $\theta$  polarization induces a surface wave that diffracts off the trailing edge as observed in radar cross section analysis [6].



(a)

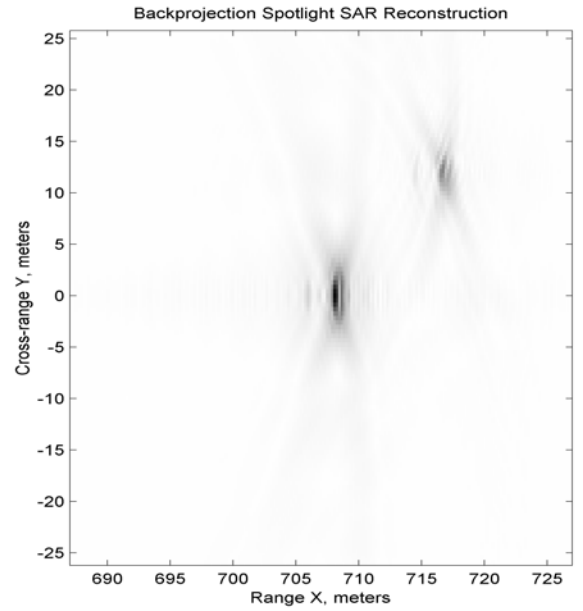


(b)

Figure 5: (a) Two-plate WIPL geometry; (b)  $E_{\phi\phi}$  backprojection spotlight SAR reconstruction.



(a)



(b)

Figure 6: (a) Two-plate WIPL geometry; (b)  $E_{\theta\theta}$  backprojection spotlight SAR reconstruction.

#### 4.1.2. Three plates

The next target scene is shown in Figure 7a. This scene now features multiple plates with varying orientations: a three meter square plate, a rotated three meter square plate, and a circular plate with a diameter of three meters. The displacement from the center of the target region of the rotated square plate is  $(\Delta x, \Delta y) = (-12, 12)$  meters and of the circular plate is  $(\Delta x, \Delta y) = (-12, -12)$  meters. The bandwidth is 400MHz between 100MHz-500MHz. The resulting backprojection spotlight SAR reconstructions are shown in Figure 7b for the  $\varphi$  polarized case and Figure 8b for the  $\theta$  polarized case. As shown in Figure 7b, the dominant reflection points of the three different targets are visible. For the non-rotated square plate and circular plate, the leading edges are seen and appear at the correct location. The range distances to the leading edges of the plates can be readily calculated as

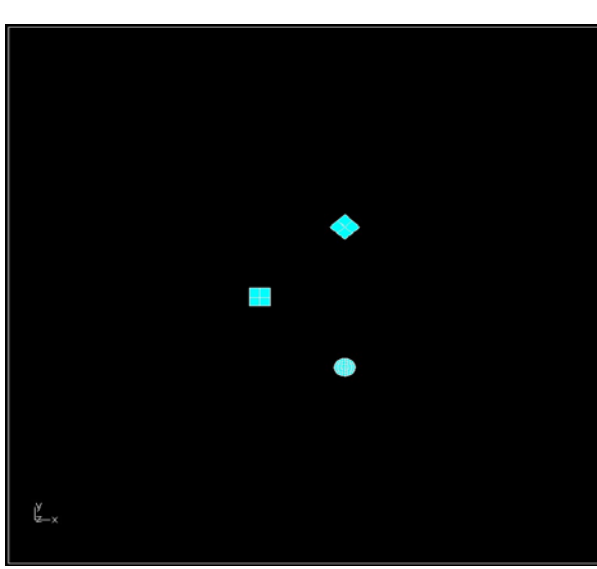
$$X_{sq} = \sqrt{((500 - 1.5)^2 + (500)^2)} = 706.1m \quad (29)$$

$$X_{circ} = \sqrt{((500 + 12 - 1.5)^2 + (500)^2)} = 714.6m \quad (30)$$

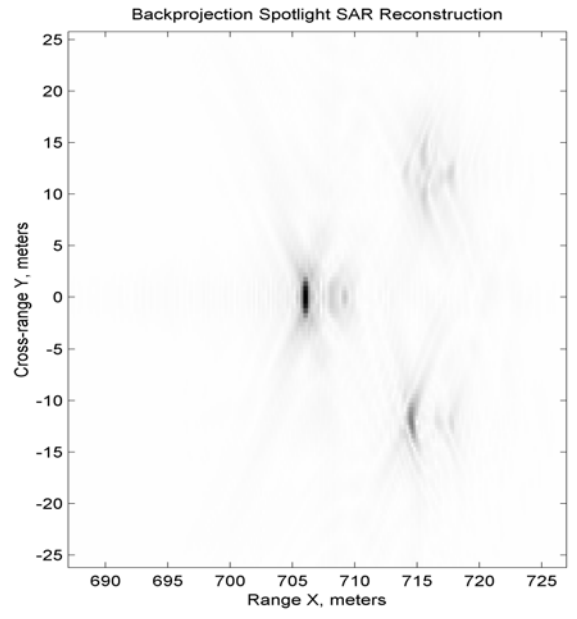
$$X_{rot\ sq} = \sqrt{((500 + 12 - 2.12)^2 + (500)^2)} = 714.1m \quad (31)$$

where the diagonal plate length is  $\sqrt{((1.5)^2 + (1.5)^2)} = 2.12m$ . The dimensions in the cross-range (about three meters) are also correct. For the rotated square plate, the dominant reflections appear at the corners of the plate. The positions of the corner reflectors appear at the range and cross-range locations corresponding to the approximate dimensions of the plate. The  $\theta$  polarized reconstruction shown in Figure 8b displays similar features to those of the Figure 6b  $\theta$  polarized reconstruction. From Figure 8b the trailing edge of non-rotated square plate, a portion near the trailing edge of the circular plate and an area near the rear corner reflector of the rotated square plate can be seen.

The basic examples shown in Figure 5 through Figure 8 demonstrate the ability to distinguish between multiple targets of varying geometry and orientation in the same target scene. The objects appear at the correct locations and with the approximately correct dimensions in the cross-range. They show the types of features which can be obtained from targets with a certain geometry and orientation. Also demonstrated is how different objects in the same scene display relative high/low RCS properties as a function of geometry and orientation. Specifically, *compare the non-rotated and rotated square plates shown in Figure 7*. Although both objects have the same dimensions, the non-rotated plate that has a flat edge oriented parallel to the synthetic aperture appears much more clearly as a result of its larger RCS. These properties will also be shown in the next section.

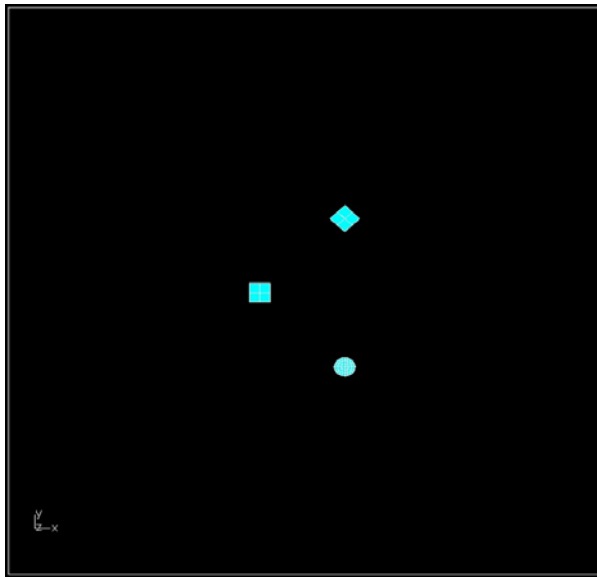


(a)

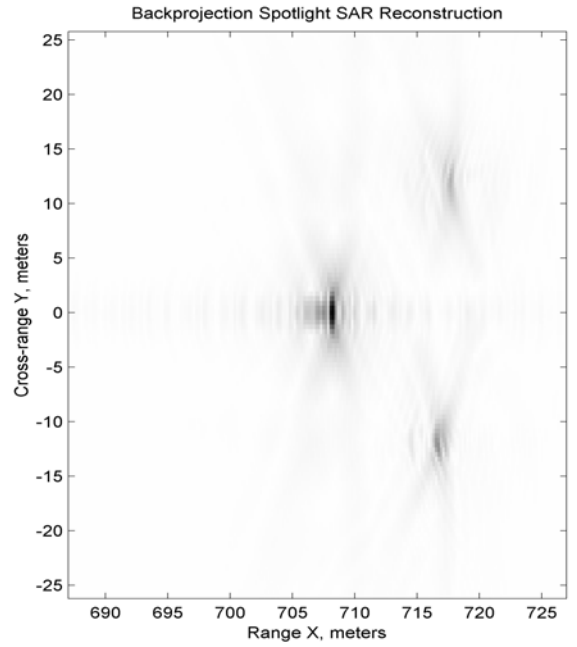


(b)

**Figure 7: (a) Three-plate WIPL geometry; (b)  $E_{\phi\phi}$  backprojection spotlight SAR reconstruction.**



(a)



(b)

**Figure 8: (a) Three-plate WIPL geometry; (b)  $E_{\theta\theta}$  backprojection spotlight SAR reconstruction.**

#### 4.1.3. Plates with ridges

The plates featured in the previous sections all have smooth surfaces and as a result the radar energy incident on the body of the plates (away from the edge discontinuities) tends to reflect away from the synthetic aperture direction. Such reflectors are termed specular reflectors. The images shown in the earlier section are consistent with such specular reflection. On the other hand, a reflector with surface roughness will reflect some fraction of the incident radar energy back towards the synthetic aperture (as well as other directions) depending on the degree of ‘roughness’. Consider next the targets shown in Figure 9. These targets are again three meter square plates but now with triangular shaped ridges added. Such reflectors are termed diffuse reflectors. The difference between smooth and rough surfaces is relative and can be related to the statistical variations in the surface height of the reflector. To exhibit roughness, the variations in the surface height should be comparable to the radar wavelength.

To demonstrate the effect of surface roughness on the reflected SAR signal (and hence the SAR reconstructed image), two plates with different degrees of surface roughness are analyzed. A plate with large ridges (four ridges with height of 37.5cm) is shown in Figure 9a, and a plate with small ridges (eight ridges with height of 18.75cm – one half the height of the large ridge plate) is shown in Figure 9b. The leading edge of both plates are located at  $X_{cc} = 707.1\text{m}$ . The triangular faces of the plate ridges are angled at  $45^\circ$  which points approximately towards the synthetic aperture. The bandwidth is still 400MHz between 100MHz-500MHz, corresponding to wavelengths between  $\lambda_{max} = 3\text{m}$  to  $\lambda_{min} = 0.6\text{m}$ .

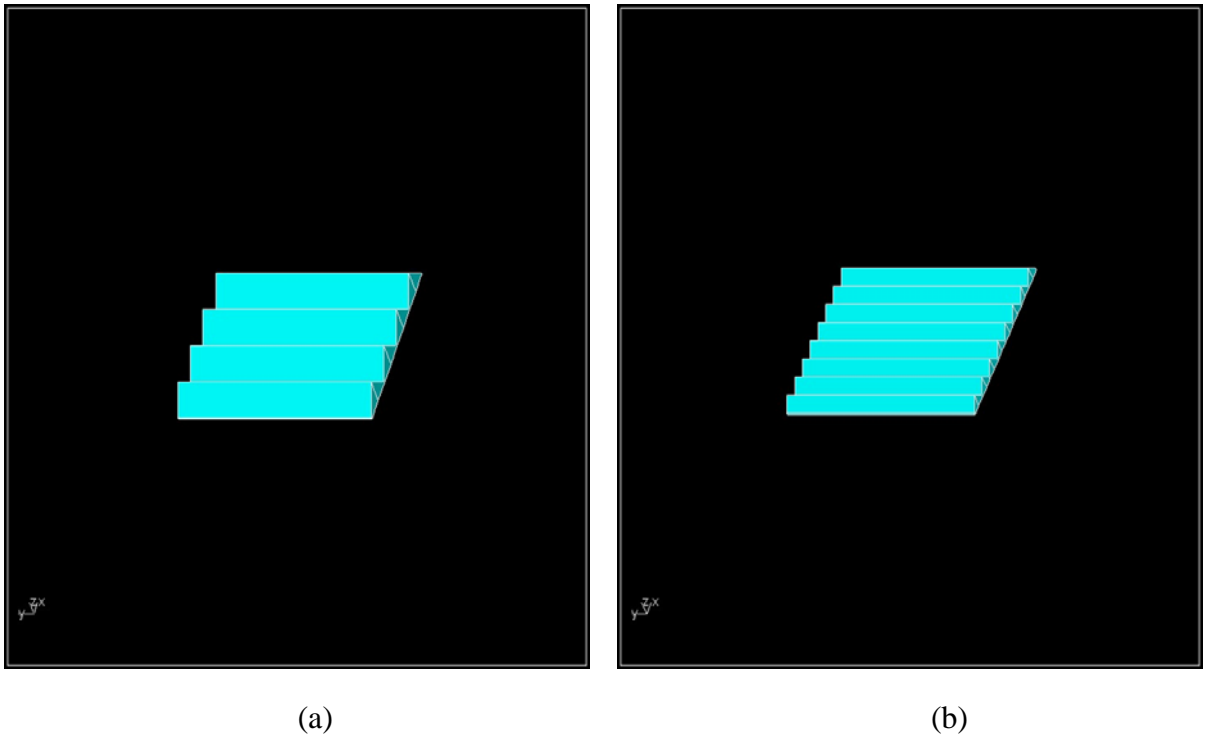


**Figure 9: Ridged plate WIPL geometry. (a) Large ridges; (b) small ridges**

The resulting backprojection spotlight SAR reconstructions are shown in Figure 10 and Figure 11 for the large and small ridged plates respectively. As shown in Figure 10, due to the increased surface roughness of the large ridged plate, most of the plate body is now visible. The location of the plate as well as the dimensions in both the cross-range *and* range can now be confirmed as correct. However, as shown in Figure 11, the plate with smaller ridges exhibits less surface roughness and as a result the plate body again disappears in the reconstruction. The reconstructed image of the small ridged plate again looks similar to that of the ‘smooth’ plates in the previous sections where only the leading edge appears. The location of the leading plate edge as well as its approximate dimension in the cross-range is still correct. The surface roughness or variation in the surface dimension has a strong effect on the backscattered field and hence the reconstruction. Only surfaces that reflect the incident field back towards the synthetic aperture will appear in the reconstruction. Strong specular scattering from smooth man-made targets strongly affects low frequency radar imaging. This effect will also be apparent in subsequent examples.

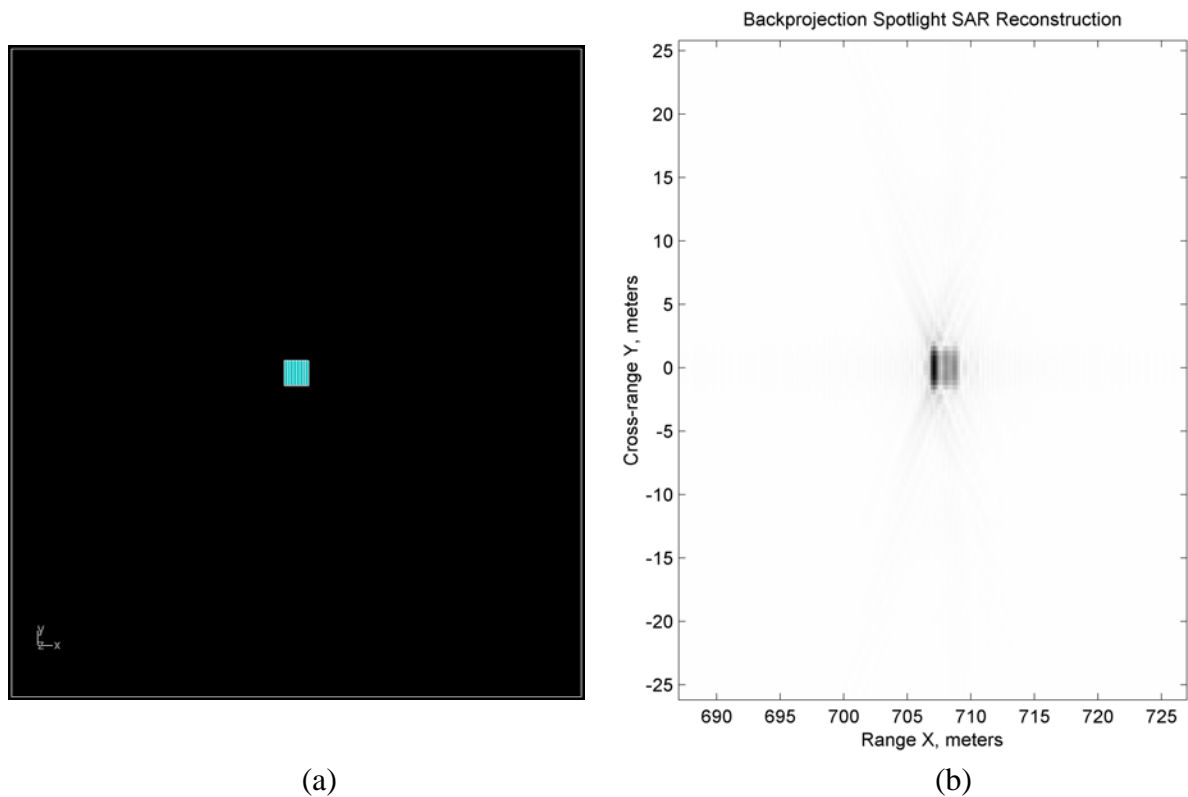


**Figure 10: (a) Large ridge plate WIPL geometry; (b)  $E_{\phi\phi}$  backprojection spotlight SAR reconstruction**

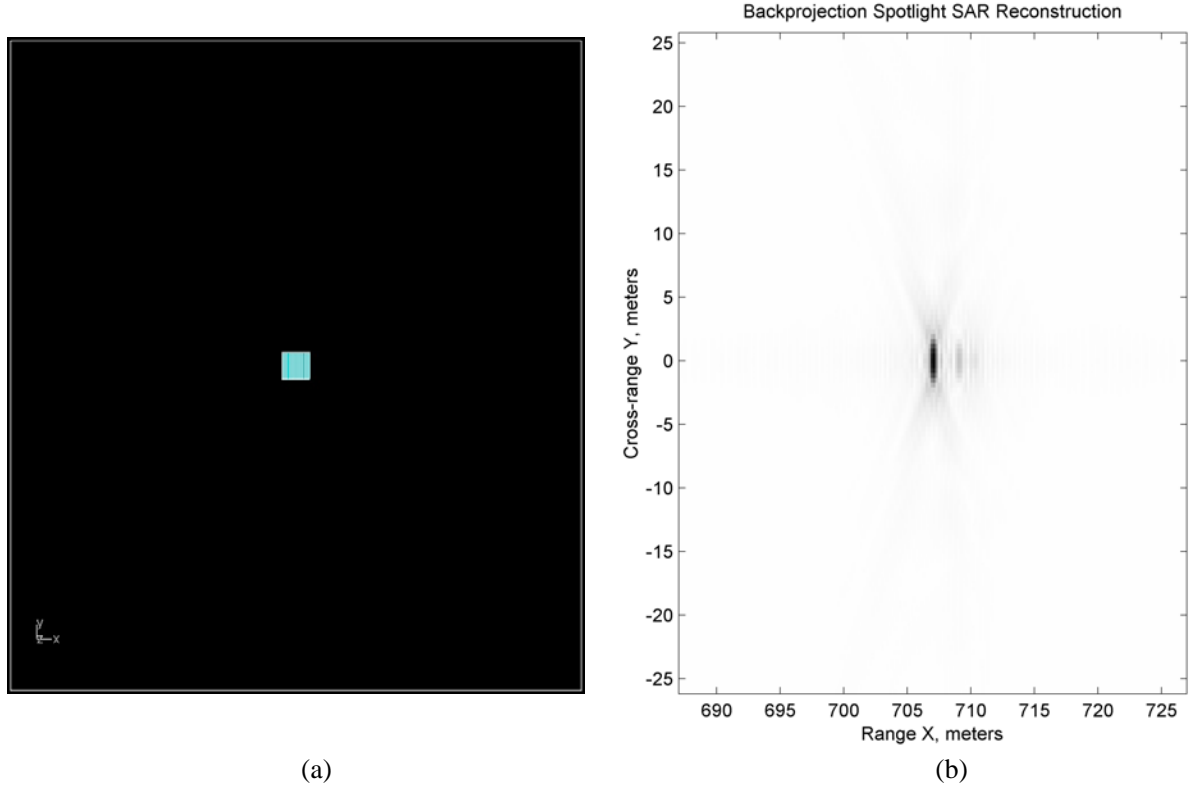


**Figure 11: (a) Small ridge plate WIPL geometry; (b)  $E_{\phi\phi}$  backprojection spotlight SAR reconstruction**

## 4.2. Advanced metal targets

### 4.2.1. Single T80 tank

Consider the three dimensional tank target shown in Figure 12. The dimensions of this tank provided in Table 2 are approximately those of a T80 series tank. The tank model was deliberately kept simple in order to permit analysis with the single processor version. The bandwidth is 250MHz between 100MHz-350MHz. The orientation of the tank for the WIPL-D simulation and the resulting  $\phi$  polarized backprojection spotlight SAR reconstruction are shown in Figure 13a and Figure 13b respectively. The SAR reconstruction shows the side of the tank chassis, the side of the tank turret, and an outline of the tank barrel. Note from the dimensions provided in Table 1 that the synthetic aperture is positioned approximately at a  $45^\circ$  angle to the target region. Hence, the tank is seen from a perspective similar to that shown in Figure 12a but from a distance of about 700 meters. The features appear at the correct range location and with the correct approximate geometry in the cross-range. For example, the center of the side of the tank turret is at an approximate range distance of

$$X_{turret} \cong \sqrt{((500-1)^2 + (500-1.9)^2)} = 705.1m \quad (32)$$

The reconstruction shows the strongest reflection from the side of the turret since its face is oriented upwards approximately towards the synthetic aperture producing the largest RCS from this location of the tank.

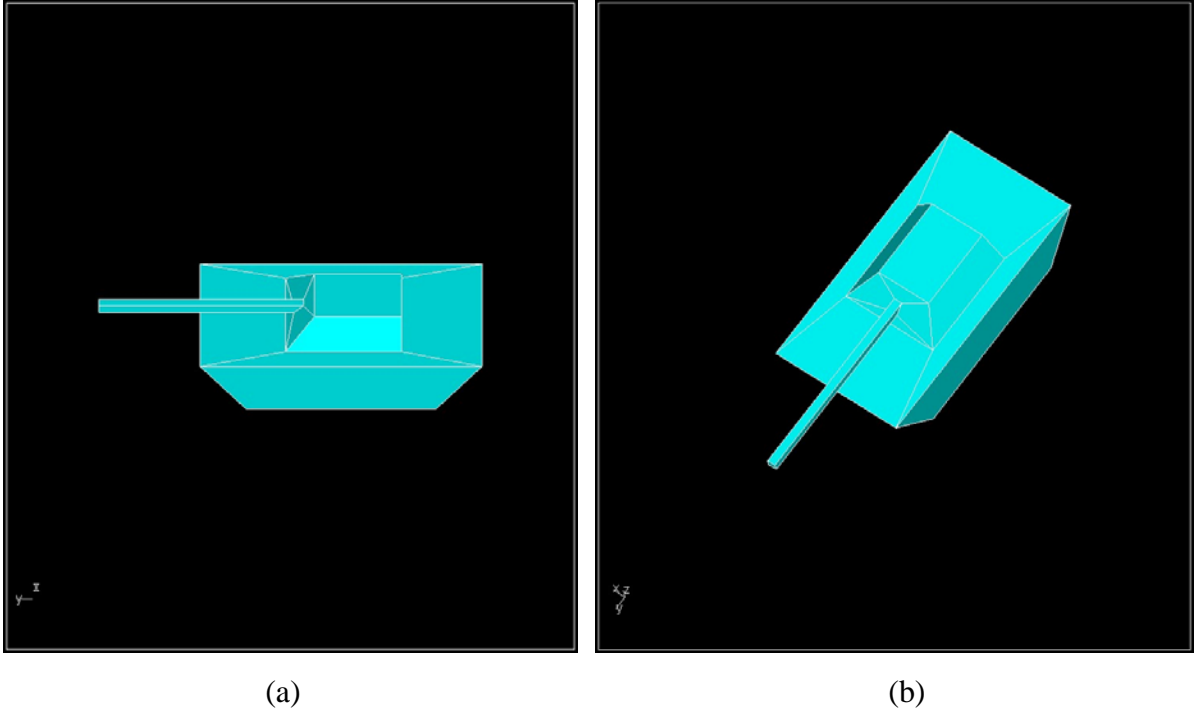


**Figure 12: T80 tank WIPL geometry**

Dimension	Size (meters)
Chassis length	7
Chassis width	3.6
Turret width	2.6
Chassis height	1.5
Total height	2.2
Barrel length	6

**Table 2: T80 tank dimensions**

The  $\theta$  polarized reconstruction is shown in Figure 14. This reconstruction shows a similar feature to previous  $E_{\theta\theta}$  polarized simulations (see Figure 6 and Figure 8) since the trailing edge of the tank chassis also appears. The leading edge of the tank chassis and outline of the tank barrel are less dominant than in the  $E_{\varphi\varphi}$  polarization reconstruction shown in Figure 13. The location and dimensions indicated by these features are again correct. The side of the tank turret appears with approximately the same intensity for both polarizations. This is probably since the plate modeling the side of the turret is facing approximately towards the synthetic aperture and reacts equally to both polarizations. Combining the information obtained from both polarizations provides significant details about the tank location and geometry.

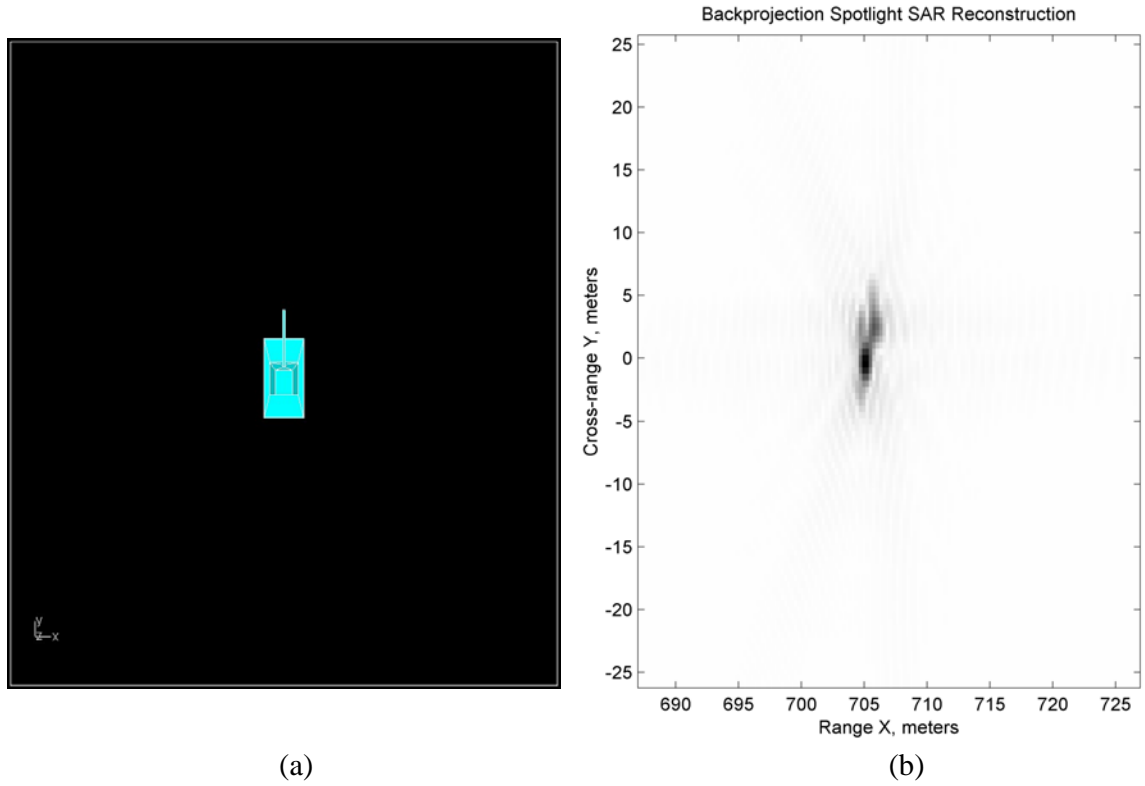


**Figure 13: (a) T80 tank WIPL geometry; (b)  $E_{\varphi\varphi}$  backprojection spotlight SAR reconstruction**

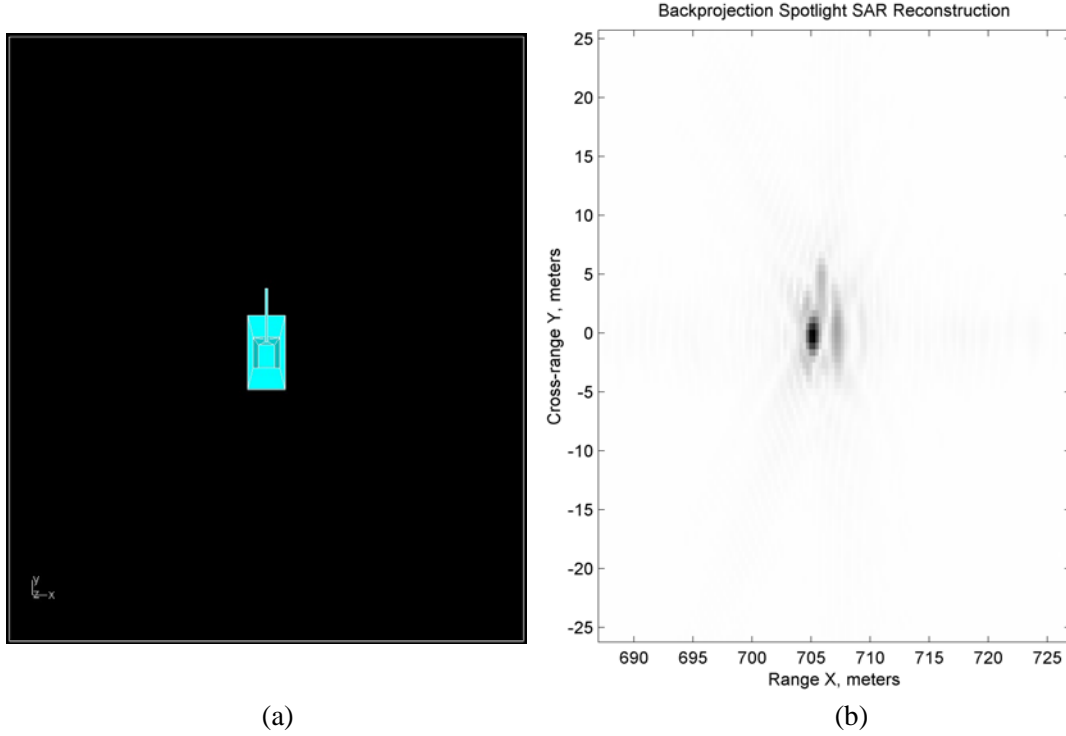


**Figure 14: (a) T80 tank WIPL geometry; (b)  $E_{\theta\theta}$  backprojection spotlight SAR reconstruction**

#### 4.2.2. Twin broadside T80 tanks

Next consider the target scene shown in Figure 15a which consists of two T80 tanks. One tank is at the center of the target region and the other tank is displaced a distance of  $(\Delta x, \Delta y) = (7, -14)$  meters. The bandwidth is 230MHz from 100MHz-330MHz. The resulting backprojection spotlight SAR reconstruction is shown in Figure 15b. The main features of the sides of both tanks can be seen: the side of the chassis and turret as well as the outline of the barrel. The approximate range location and cross-range dimension of both tanks is correct. The image of the displaced tank is slightly different compared to the central tank since the synthetic aperture view of the displaced tank is slightly different.

#### 4.2.3. Twin rotated T80 tanks

Finally, consider the target geometry shown in Figure 16a which again consists of two T80 tanks. The first tank is at the center of the target region and the second tank is still displaced a distance of  $(\Delta x, \Delta y) = (7, -14)$  meters but now is also rotated by  $30^\circ$ . The bandwidth is still 230MHz from 100MHz-330MHz. The resulting backprojection spotlight SAR reconstruction is shown in Figure 16b. The main features of the first tank at the center of the target region are still visible as with the reconstruction shown in Figure 15b. However, the displaced and rotated second tank is only partially visible and any obvious features cannot be extracted.

Since the displaced tank is now rotated, the side of the tank chassis and turret which both constituted strong broadside reflectors is no longer facing towards the synthetic aperture. As a result, the RCS of the

rotated tank is significantly reduced compared to the tank at the center of the target region and hence fades in the reconstruction. This effect is analogous to that seen for the rotated square plate in Figure 7.

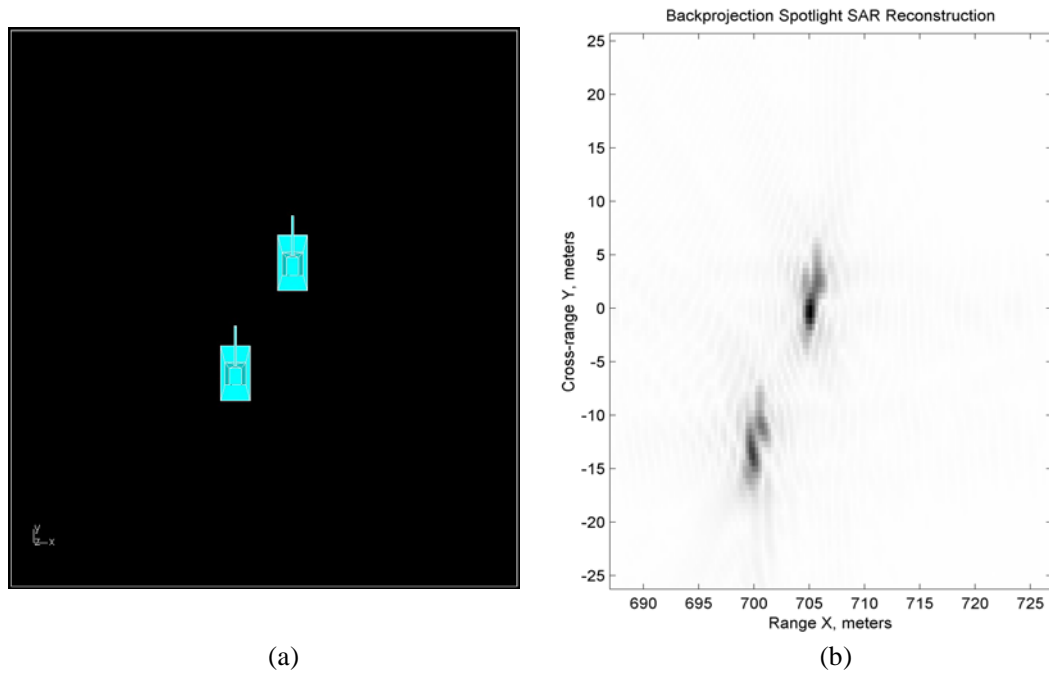


**Figure 15: (a) Broadside twin T80 tank WIPL geometry; (b) backprojection spotlight SAR reconstruction.**

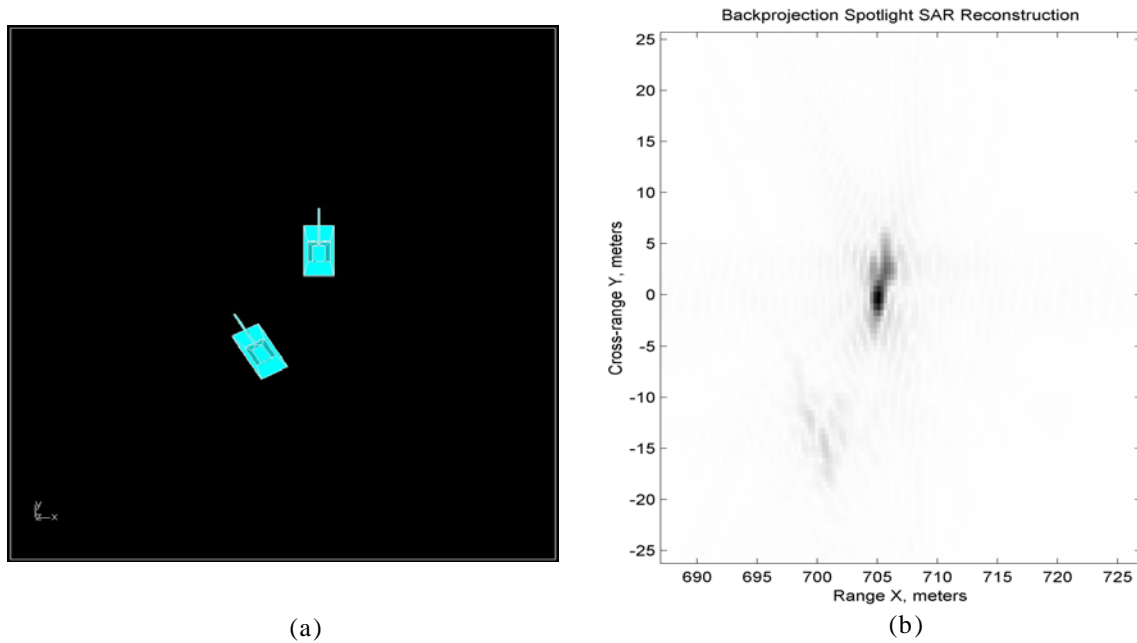


**Figure 16: (a) Rotated twin T80 WIPL geometry; (b) backprojection spotlight SAR reconstruction**

An explanation of these results is also obtained from plotting the SAR signal after matched filtering in the slant range (fast-time). The time domain SAR signal along the aperture after matched filtering is shown in Figure 17a and Figure 17b for the geometries of Figure 15 and Figure 16 respectively. In Figure 17a, there are two clearly visible SAR wavefronts corresponding to the two tanks. However, in Figure 17b, there is only one clear SAR wavefront that corresponds to the tank at the center of the target region. The second weaker SAR wavefront corresponds to the rotated tank. Its amplitude is significantly reduced and is only visible over the lower part of the aperture where the side of rotated tank chassis and turret are oriented closer to broadside relative to the lower part of the synthetic aperture.

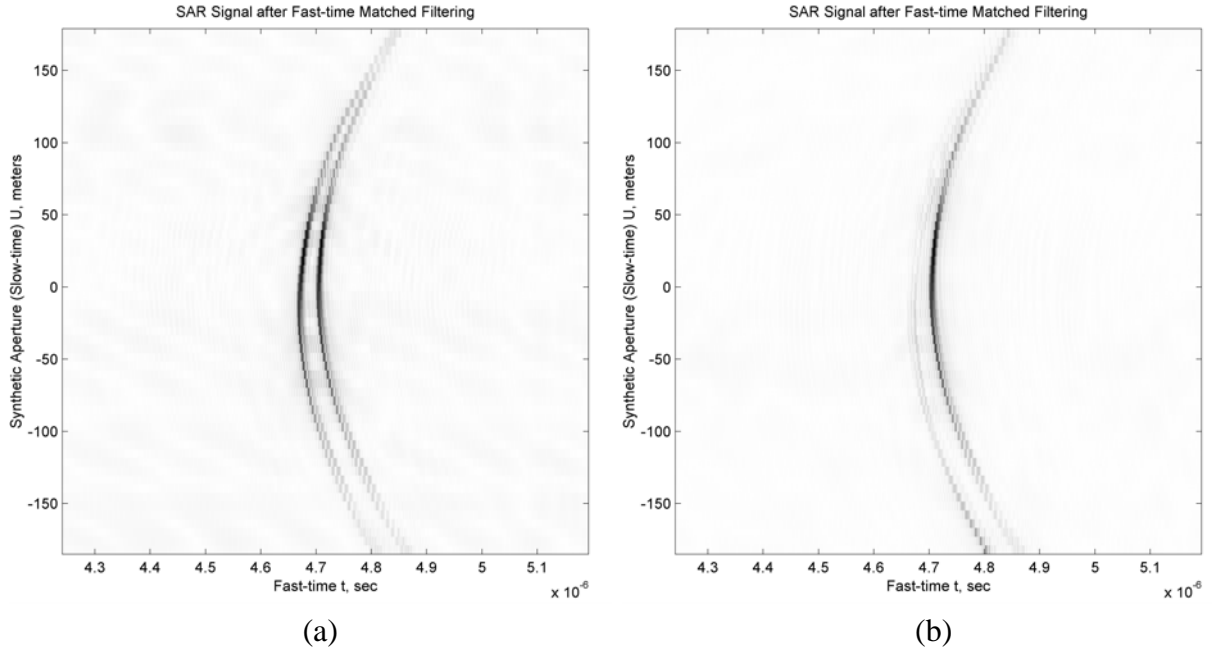


**Figure 17: Time-domain SAR signal after matched filtering. (a) Broadside twin T80 simulation; (b) rotated twin T80 simulation**

## 5.0 Target examples involving foliage

This section gives the results for SAR images of an STR consisting of dielectric targets and dielectric targets combined with metal targets. The same SAR dimensions provided in Table 1 are retained for these examples. In the first example, a scene composed entirely of dielectrics is discussed. In the subsequent examples, scenes with dielectric and metal targets are shown. All of these example scenes are very simple and employ very simple foliage models. This was necessary to enable analysis with the single processor version. The purpose of these basic examples is to confirm WIPL-D's ability to accurately analyze regions including both dielectric and metal regions.

### 5.1. A simple tree model

Consider the scene shown in Figure 18 of a tree. As with the tank, to reduce the number of unknowns the tree model has been kept basic: it is simply modeled as two different dielectric regions and it has no distinct branches. The height of the tree is 4.4 meters. The branch body of the tree has a relative permittivity of  $\epsilon_r = 6$  and the trunk has a relative permittivity of  $\epsilon_r = 7$ . The branch body and trunk of the tree are modeled as being solid. The dimensions and permittivity assignments of the tree are summarized in Figure 19. Note that more complex foliage models could also be implemented at the expense of computational complexity. This will be examined later in Section 5.4.

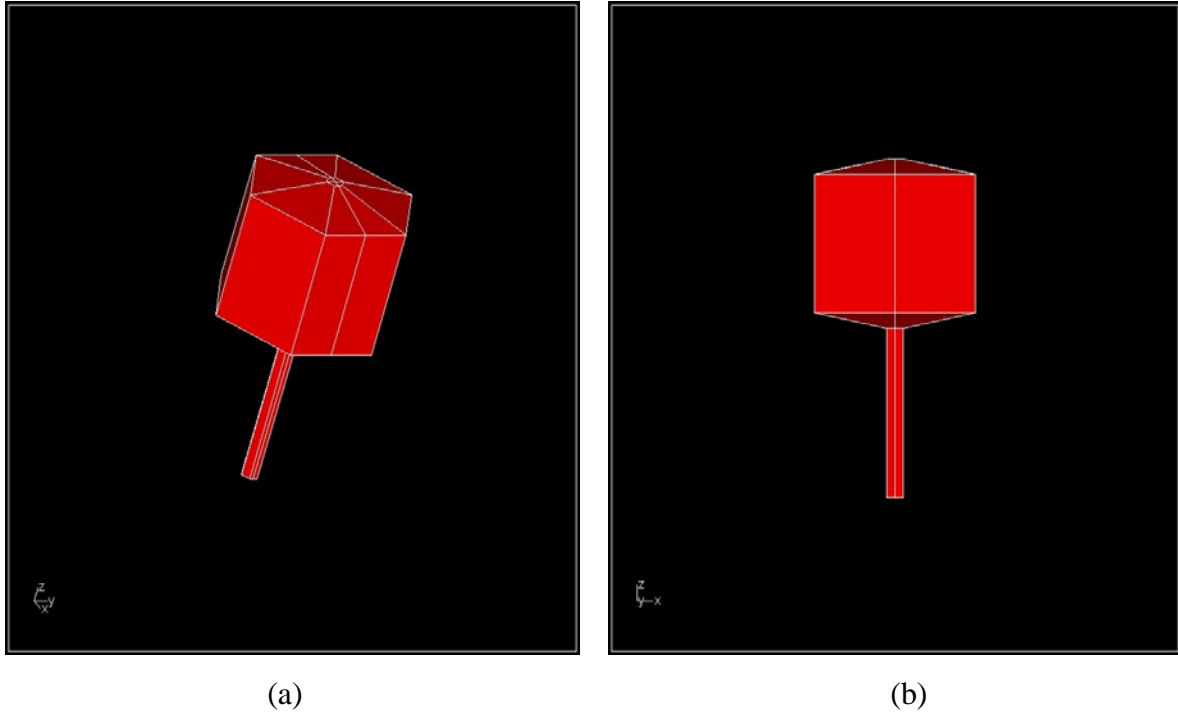


**Figure 18: A dielectric tree target**

The backprojection spotlight SAR reconstruction is shown in Figure 20 for a bandwidth of 230MHz from 100MHz-330MHz. Note the multiple dark regions that appear in the reconstruction. This is likely a result of the multiple reflections that occur within the dielectric body of the tree. These multiple reflections are apparent in the time domain SAR signal along the aperture obtained after matched filtering as shown in Figure 21. The appearance of multiple reflections makes the processing more difficult because reconstruction algorithms will interpret the additional wavefronts as additional scatterers. *It is precisely the scattering characteristics of dielectric structures like this that the proposed WIPL-D parallel scene generation tool will help predict.*

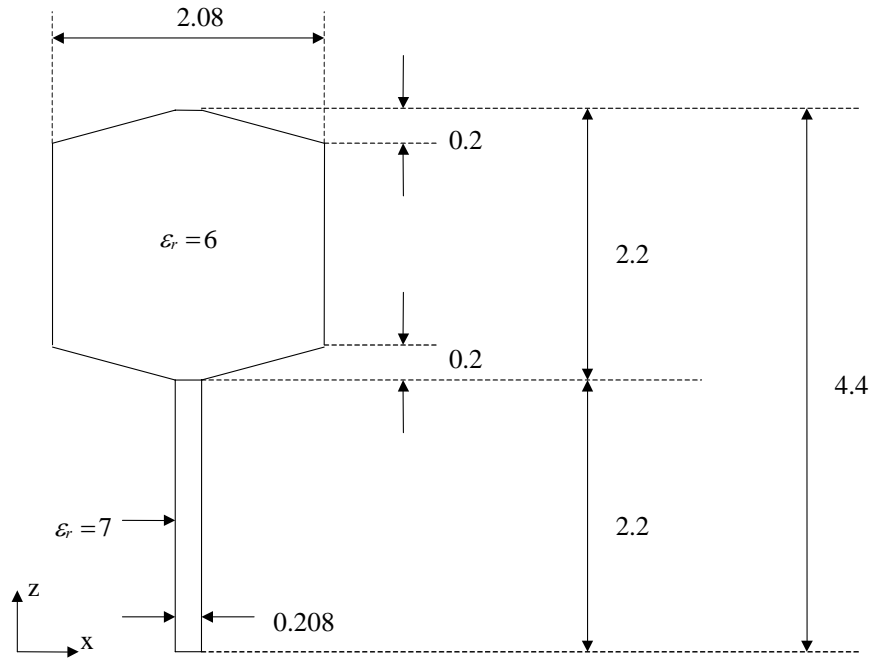


Figure 19: Tree dimensions and permittivity assignments

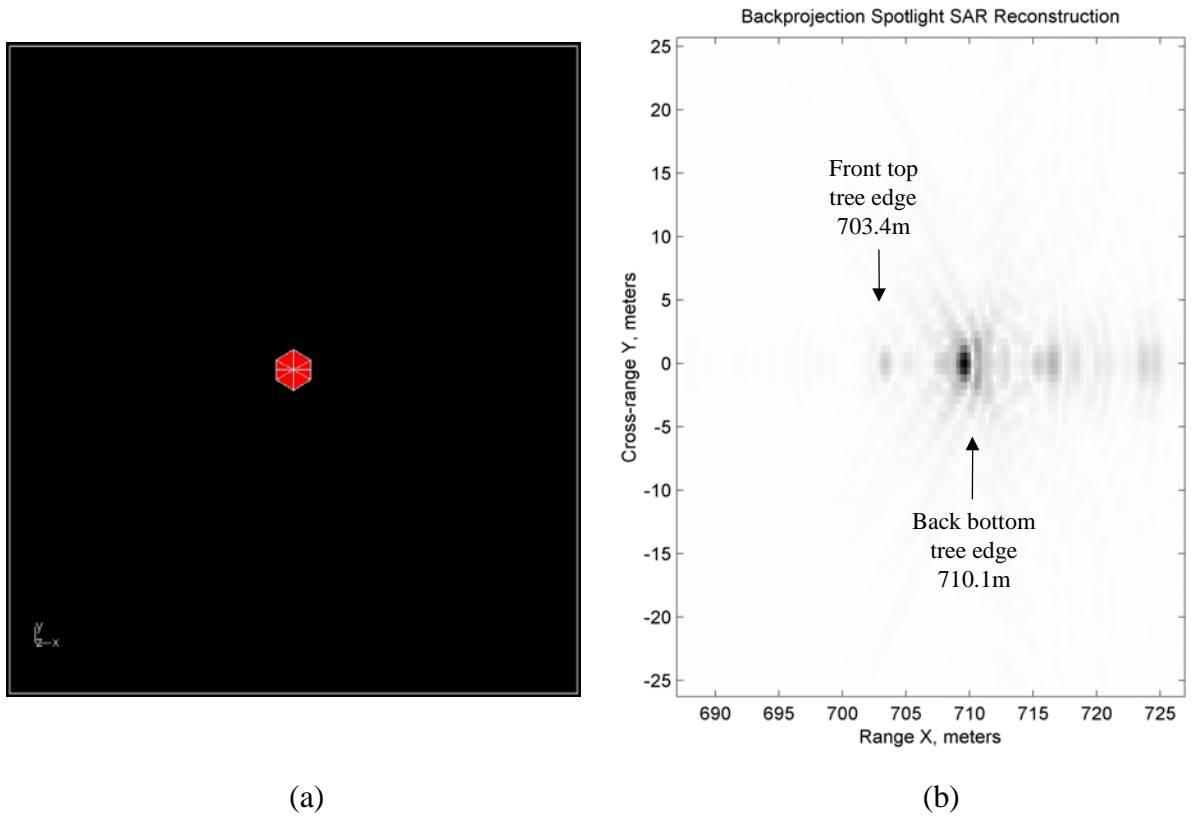
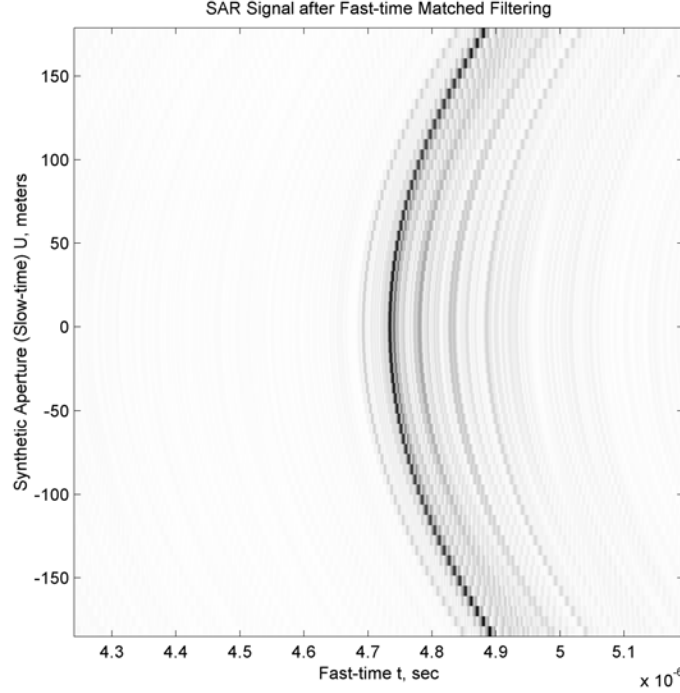


Figure 20: (a) Dielectric tree WIPL geometry; (b) backprojection spotlight SAR reconstruction



**Figure 21: Time-domain SAR signal for the dielectric tree after matched filtering**

The bottom center of the tree trunk is at the coordinate origin. The small dark area at 703 meters corresponds approximately to the front top tree edge since

$$R = \sqrt{\left(500 - \frac{2.08}{2}\right)^2 + (500 - 4.2)^2} = 703.4m \quad (33)$$

However, the main dark area doesn't directly follow the same relationship. The dark area corresponds to the back bottom tree edge. The additional distance from the front top tree edge to the back bottom tree edge is

$$\Delta R = \sqrt{(2.08)^2 + (1.8)^2} = 2.75m \quad (34)$$

The distance is taken approximately diagonally through the tree body since recall that the tree is seen at about a  $45^\circ$  angle from the synthetic aperture. According to this, the back of the tree should be near  $R + \Delta R = 706.15m$ . However, the back of the tree is closer to 710 meters. The likely cause of this is the additional phase shift (time-delay) within the dielectric body of the tree. The additional phase lag compared with free-space to the back bottom tree edge is

$$\sqrt{\epsilon_r} \Delta R = \sqrt{6} \Delta R = 6.74m \quad (35)$$

Which places the back of the tree edge near  $R + \sqrt{\epsilon_r} \Delta R \cong 710.1m$ . Almost all SAR reconstruction algorithms (including backprojection) rely primarily upon the reflected wave phase (time shift). Hence, the additional phase-lag makes the back bottom tree edge seem further away by this value.

## 5.2. A scene with dielectric and basic metal targets: Trihedral corner reflector and dielectric tree.

A scene that includes both metal and dielectric targets is shown in Figure 22. This scene consists of a metal triangular trihedral corner reflector and the dielectric tree of the previous section. The dimensions of the dielectric tree are the same and the trihedral corner has three-meter length edges. The tree has been positioned directly in front of the trihedral corner blocking most of it from the synthetic aperture view as shown in Figure 22a. The bottom center of the tree trunk is at the coordinate origin and the main trihedral corner point is shifted ahead in the x-direction a distance of 3.3 meters. The trihedral corner's axis of symmetry has been aligned approximately towards the synthetic aperture direction. The simulated bandwidth is 230MHz from 100MHz-330MHz.

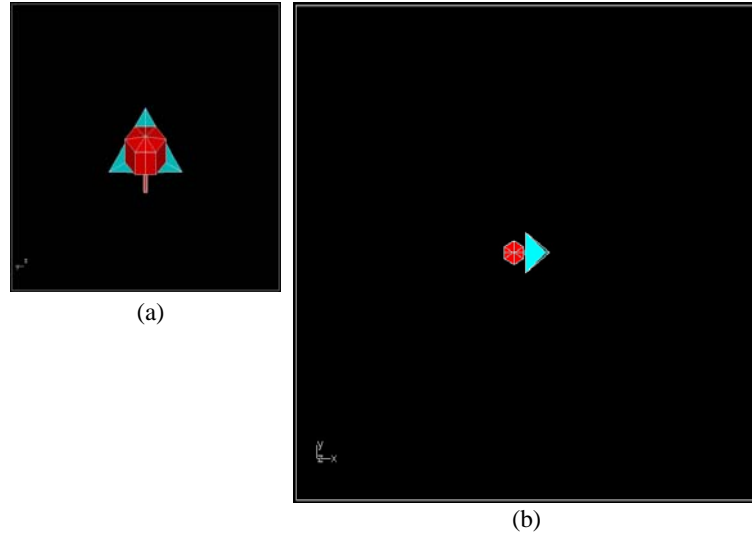


**Figure 22: Trihedral corner reflector and dielectric tree WIPL geometry**

The  $\phi$  polarized backprojection spotlight SAR reconstruction for the trihedral corner alone is shown in Figure 23. The strong reflection from the main trihedral corner point is seen and appears at the correct range location

$$X_{tri} \cong \sqrt{((500 + 3.3)^2 + (500)^2)} = 709.4m \quad (36)$$

The lower leading edge of the trihedral corner also appears, seen as a straight line at a range location of about 707.5 meters. The  $\phi$  polarized backprojection spotlight SAR reconstruction for the trihedral corner and dielectric tree of Figure 22 is shown in Figure 24. The small dark area corresponding to the front top tree edge still appears near 703.4 meters. The dark area that likely represents the back bottom tree edge is again shifted back near 710 meters as observed in Figure 20. Reflection from the main trihedral corner point is also partially visible through the tree and is also shifted back compared to Figure

23. The lower leading edge of the trihedral corner is also visible near 708 meters since it is only partially obscured by the tree and thus appears more clearly. The analysis of the foliage induced distortion of target primitives like plates, dihedral/trihedral corners etc. (of which larger structures can be seen to be composed) can be achieved using this technique.

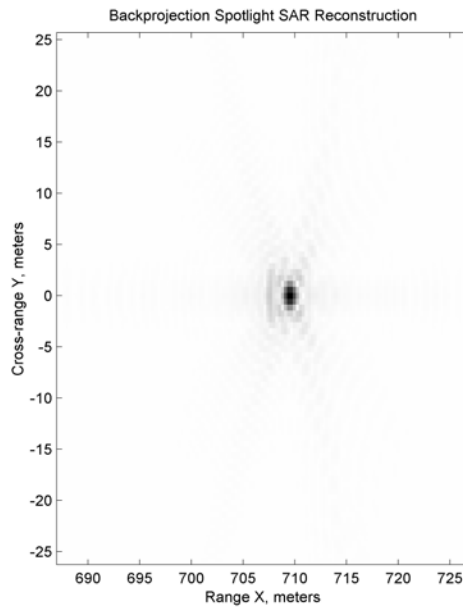


**Figure 23: Trihedral corner reflector  $E_{\varphi\varphi}$  backprojection spotlight SAR reconstruction.**

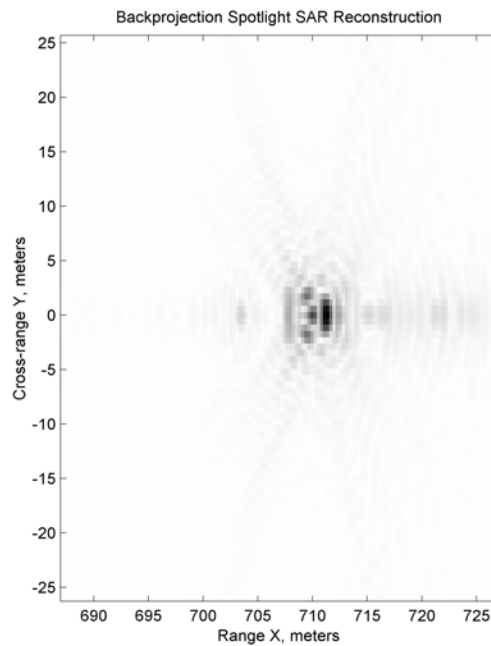


**Figure 24: Trihedral corner and dielectric tree  $E_{\varphi\varphi}$  backprojection spotlight SAR reconstruction.**

### 5.3. A scene with dielectric and metal targets: T80 tank and simple tree model

Consider next the target scene shown in Figure 25. It consists of the T80 tank discussed in Section 4.2 (advanced metal targets) and the simple tree model. All dimensions have been kept the same as in the previous simulations. The tree has been positioned directly in front of the side of the tank to obscure the view of the tank from the synthetic aperture. Its purpose is to demonstrate the effect of a general dielectric tree object on the reconstruction.

The bandwidth is 230MHz from 100MHz-330MHz. The bandwidth was deliberately reduced (compared to 250MHz for the single T80 simulation) in order to reduce the simulation time. Until the parallel version of WIPL-D (WIPL-DP) is available, the number of unknowns in the scenes to be analyzed must be kept manageable to allow reasonable run times on a single processor. The number of unknowns at the maximum frequency of 330MHz is 7445. This simulation took more than three weeks to cover the 230MHz analysis bandwidth. Since the bandwidth was reduced, the backprojection spotlight SAR reconstruction of the T80 tank using the same bandwidth of 230MHz is provided in Figure 26 for reference.

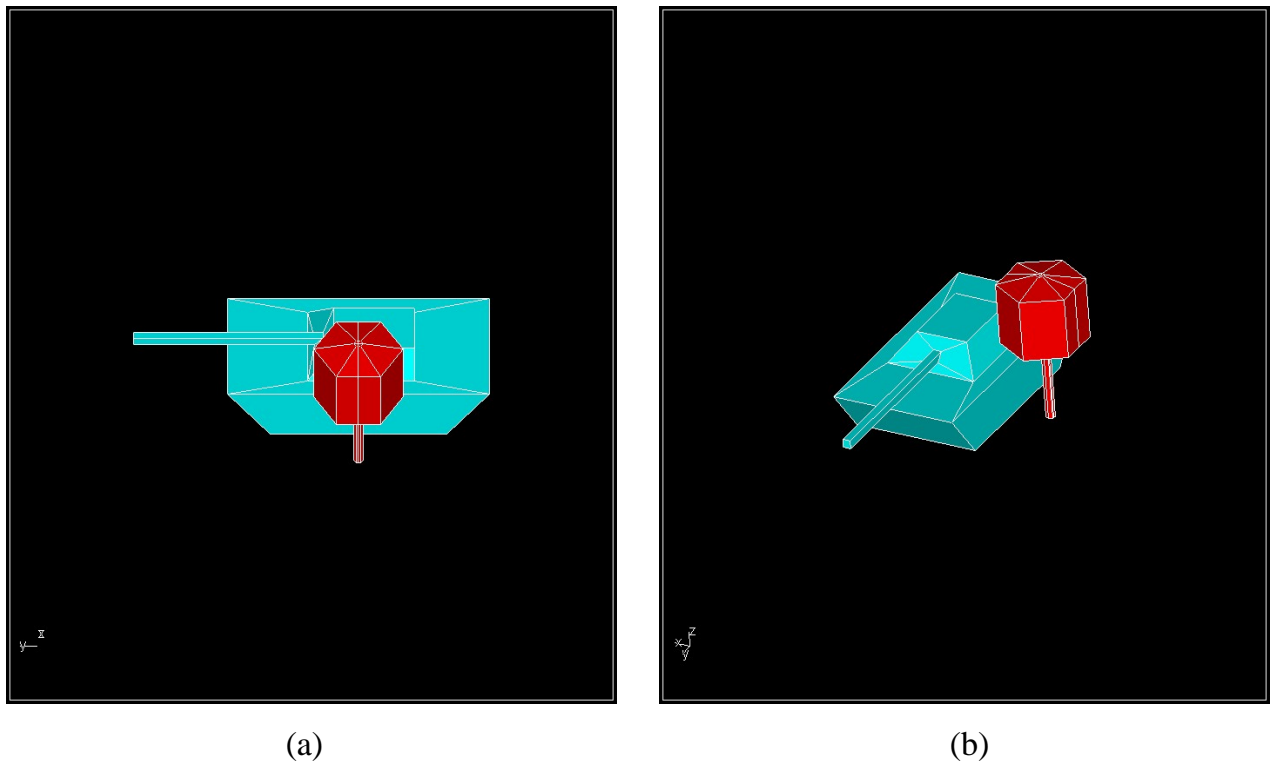


**Figure 25: T80 tank and dielectric tree geometry**

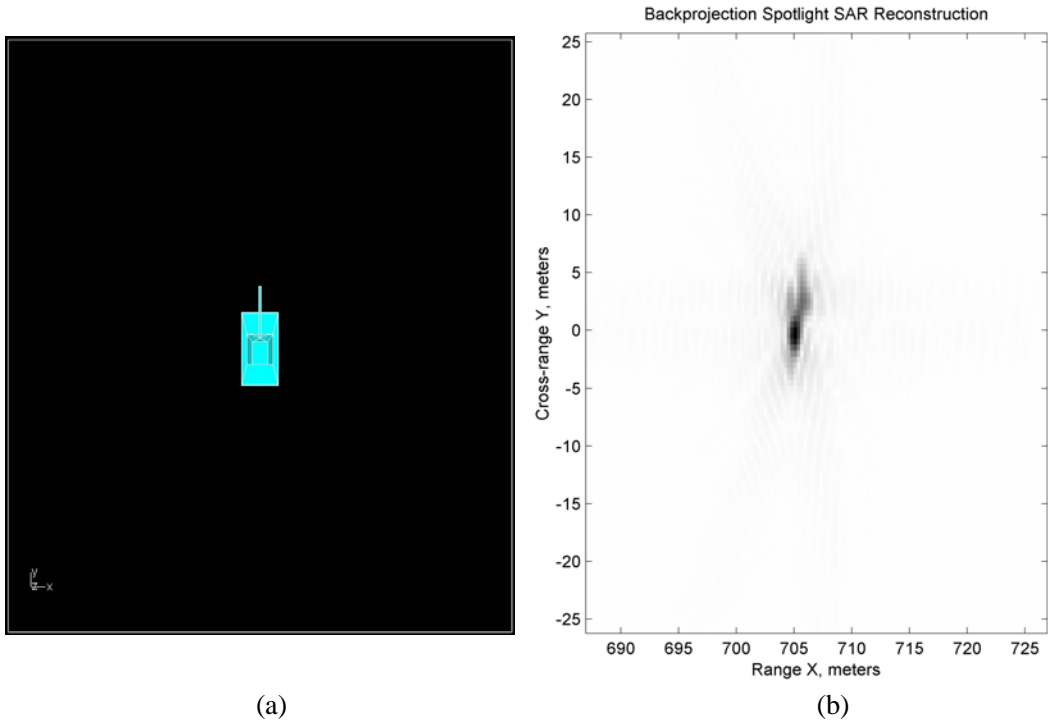


**Figure 26: (a) T80 tank WIPL geometry; (b) backprojection spotlight SAR reconstruction**

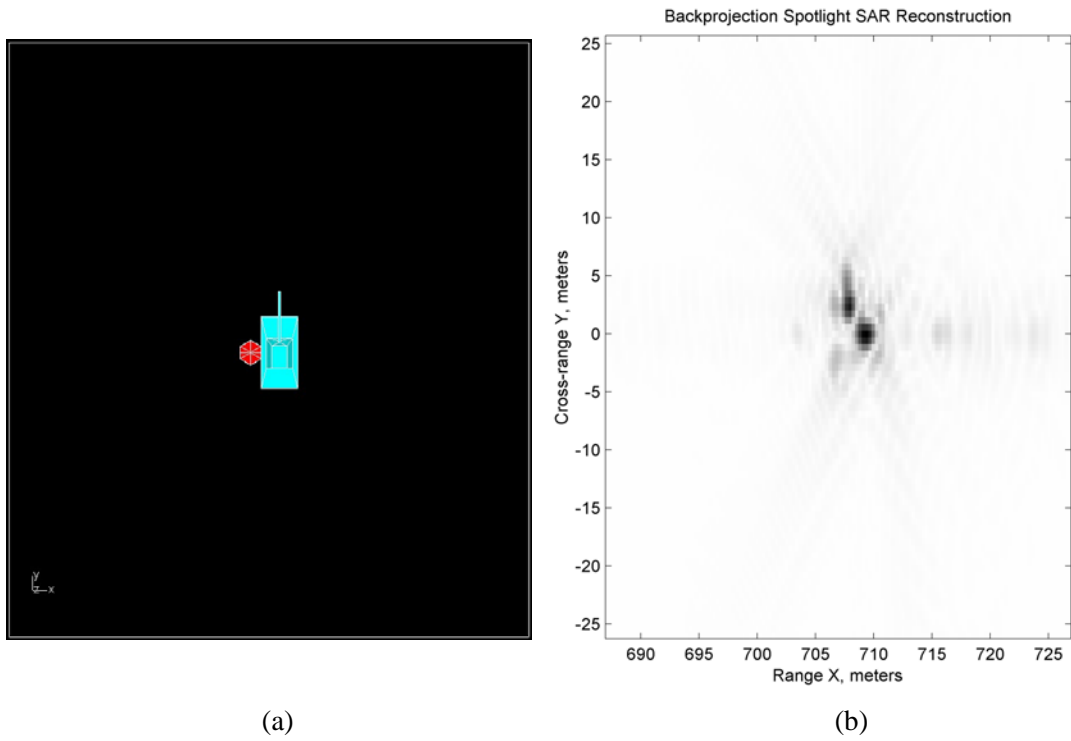


**Figure 27: (a) T80 tank and dielectric tree WIPL geometry; (b) backprojection spotlight SAR reconstruction. Compare with Figure 20b and Figure 26b.**

The backprojection spotlight SAR reconstruction for the geometry of Figure 25 is shown in Figure 27. Comparing to Figure 26, the SAR reconstructed image still shows the barrel outline and a portion of the side of the tank chassis near the front and rear of the tank. However, the side of the tank turret is missing. That is, the part of the tank the tree is directly blocking from the synthetic aperture view is gone. Recall that the synthetic aperture views the target scene from approximately a  $45^\circ$  angle similar to that shown in Figure 25a. Replacing the section of the image where the side of the tank turret resided is an image similar to that of the reconstructed tree shown in Figure 20. The dark area that likely represented the back of the tree is again shifted back as in Figure 20. The main dark area which is the side of the tank turret in the tank image of Figure 26 may also be combined with the dark area of the back of the tree seen in Figure 27. That is, the side of the tank turret may be seen ‘through’ the body of the tree also causing it to be shifted back in the image. Further analysis of scenes such as this involving metal targets obscured by arbitrary dielectric structures could also be accomplished. These basic examples successfully confirm WIPL-D’s analysis capabilities for scenes involving both metal and dielectric regions. The next example presents a scenario that is of interest in practice.

#### 5.4. A practical FOPEN scene

The target scene shown in Figure 28 represents a more practical FOPEN type situation. The tree model is now comprised of a main trunk and individual branches since in a practical FOPEN situation most of the scattering occurs from these features. Also included is a dielectric ground plane since the effect of ground bounce on the reconstructed image is significant. The trees have a height of 6m and the ground plane is 20m by 20m. The tree and ground are both assigned a permittivity of  $\epsilon_r = 7$  and a conductivity of  $\sigma = 0.01$  S/m, although both of these values can be readily altered to suit the SAR scene being investigated. The SAR dimensions are  $X'=Z=40m$ ,  $X_{cc}=56.6m$ ,  $X_0=Y_0=12m$  and  $L=14.6m$  (still corresponding to approximately a  $\pm 20^\circ$  angular range in  $\phi$  about the STR). The frequency spacing is  $\Delta f = 4\text{MHz}$  and the pulse width is  $T_p = 0.05\mu\text{sec}$ . The synthetic aperture is brought closer to the STR to enable a larger  $\Delta f$  to be used so that less simulation points are required. The simulated bandwidth is 84MHz between 40MHz-124MHz.

The backprojection spotlight SAR reconstruction for this scene is shown in Figure 29. Although the image resolution is low due to the reduced bandwidth used, a dark area localized around the tank position can still be identified. The presence of the dielectric trees has little observable affect on the reconstruction as a result of the frequency range employed. That is, the radar signal is largely penetrating the foliage at these frequencies. The reconstruction over a larger frequency bandwidth would increase the image resolution but the effect of the foliage would become increasingly apparent. Simulating over a larger bandwidth than this would require a prohibitive amount of time for a single processor analysis. The usage of multiple processors in parallel would remove this limitation. The maximum number of unknowns (10,000) for the single processor version was reached for this example at the highest frequency point of 124MHz.

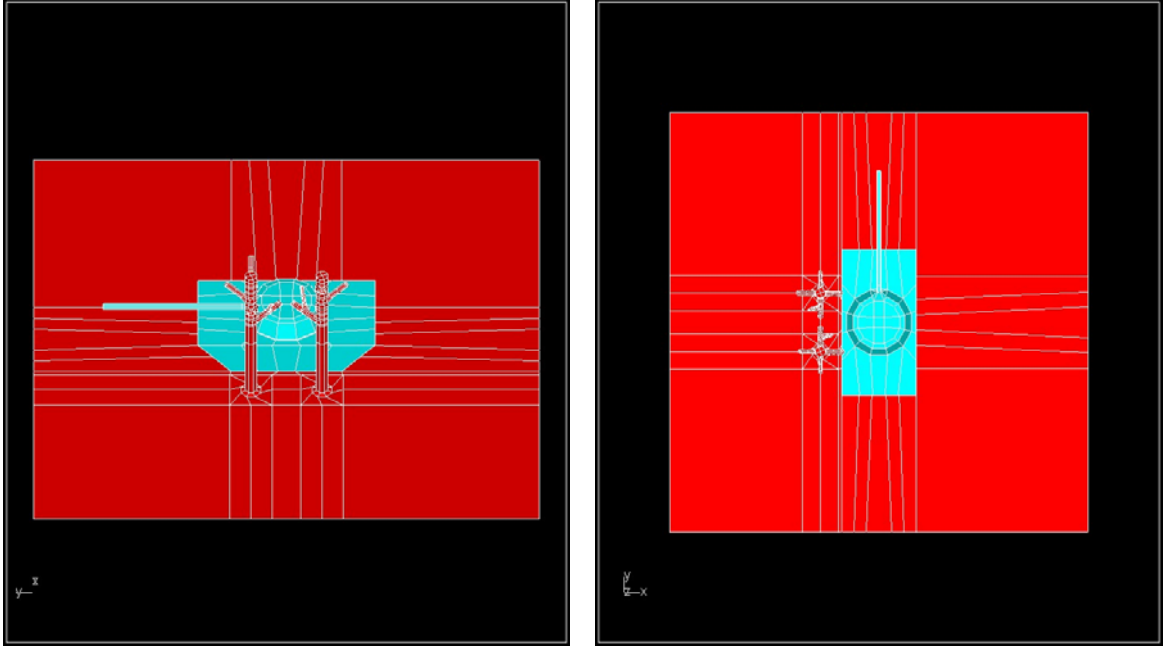


**Figure 28: A practical FOPEN scene featuring a tank with dielectric trees and ground plane.**

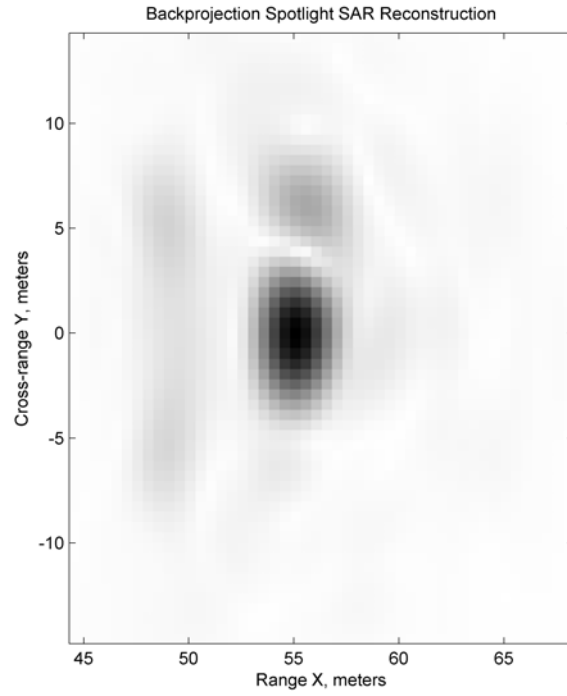


**Figure 29: Practical FOPEN scene backprojection spotlight SAR  $E_{\varphi\varphi}$  reconstruction.**

## 6.0 Linear Superposition Approach

Using this approach, each scattering object in a target scene is simulated separately to reduce the total number of unknowns and runtime. The total scattered field is then calculated by superposition of the individual scattering objects. The translated objects change in phase is used to calculate its contribution to the total received field at each aperture point. This approach essentially enables the reuse of scattered field data from previously simulated objects. This approach is valid if the electromagnetic interaction between objects in the target scene is not significant. Of course, the interaction between some targets and their environment (for example, between the foliage and tank) can be very significant as was demonstrated. However, this approach could be used to simulate smaller sub-sections of a target scene in isolation, where the electromagnetic interaction is not significant, and then combine the results into the complete scene.

The first example of this approach is shown in Figure 30 that is the broadside twin T80 simulation scene shown in Figure 15. In Figure 30a, the backprojection spotlight SAR reconstruction is shown using data obtained from a WIPL simulation with both T80 tanks included in the same scene. In Figure 30b, the backprojection spotlight SAR reconstruction is shown using superposition of data obtained from the WIPL simulation of a single T80 tank. As can be seen, the two reconstructions are virtually identical. Since the reconstruction in Figure 30b only used the scattering data from a single T80 tank in isolation, there is a significant reduction in simulation time. The simulation is still very realistic, capturing target aspect angle and relative location dependence on the reconstruction. However, these results are only valid since the electromagnetic interaction between the two T80 tanks is small. If the two T80 tanks were placed closer together or if one of the tanks blocked the synthetic aperture's view of the other then this approach would not produce correct results.

The next example of this approach is shown in Figure 31 that features the T80 tank and a sparse 'forest' composed of the basic dielectric tree model presented previously. In this application of superposition, since the interaction between the central T80 tank and the dielectric tree blocking it is significant as demonstrated in previous simulations, these scattering objects are simulated together. The electromagnetic interaction between the sparsely separated trees is likely small and so the scattered field from a single tree in isolation is used to calculate its contribution to the total scattered field. Applying superposition, the scattered field from the T80 tank and dielectric tree together and from each of the isolated dielectric trees can be used to calculate the total scattered field at each particular aperture point. The resulting backprojection spotlight SAR reconstruction using this approach is shown in Figure 32. This approach could be used to simulate isolated packets of more densely spaced foliage near a tank target and then combined to form a larger scene.

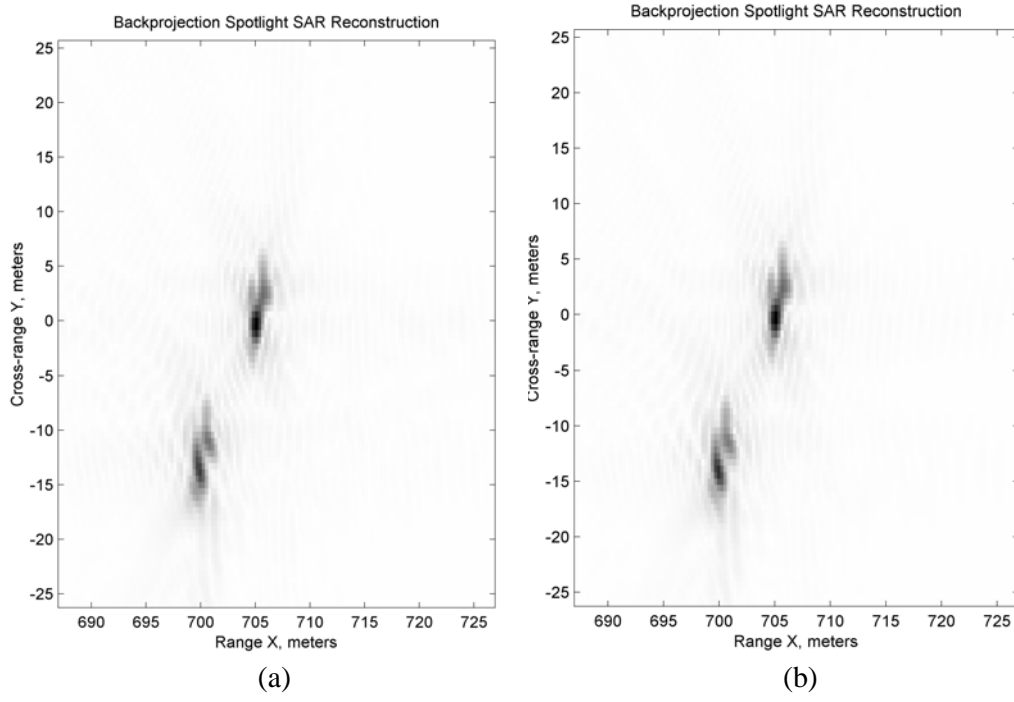


**Figure 30: Twin T80 backprojection spotlight SAR  $E_{\phi\phi}$  reconstruction. (a) Simulating both T80 tanks in the same scene; (b) Using superposition from a single T80 simulation.**

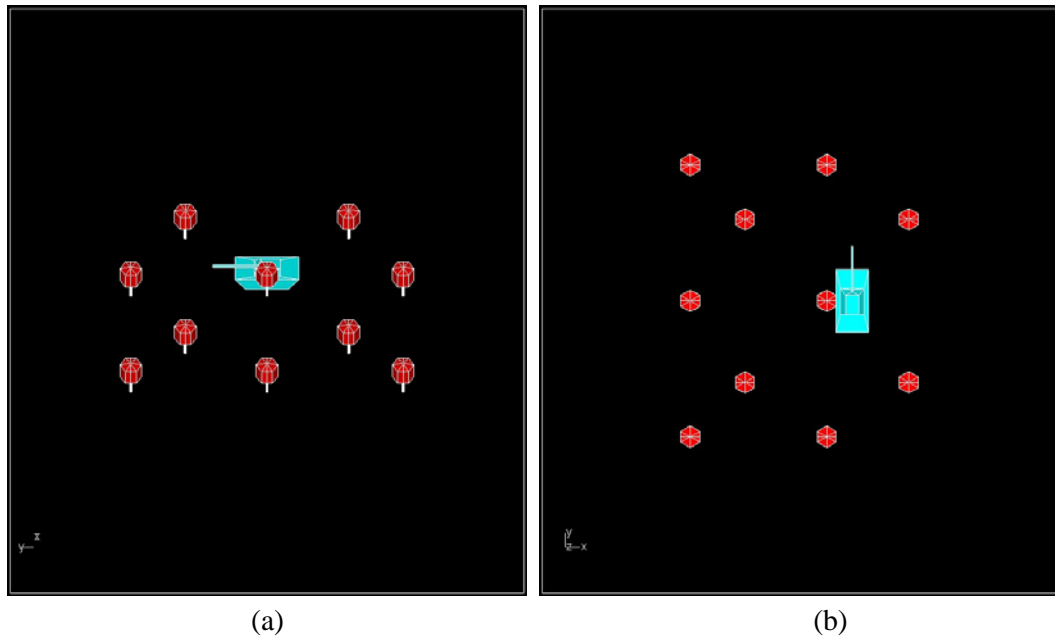


**Figure 31: T80 tank and dielectric tree sparse forest WIPL geometry.**

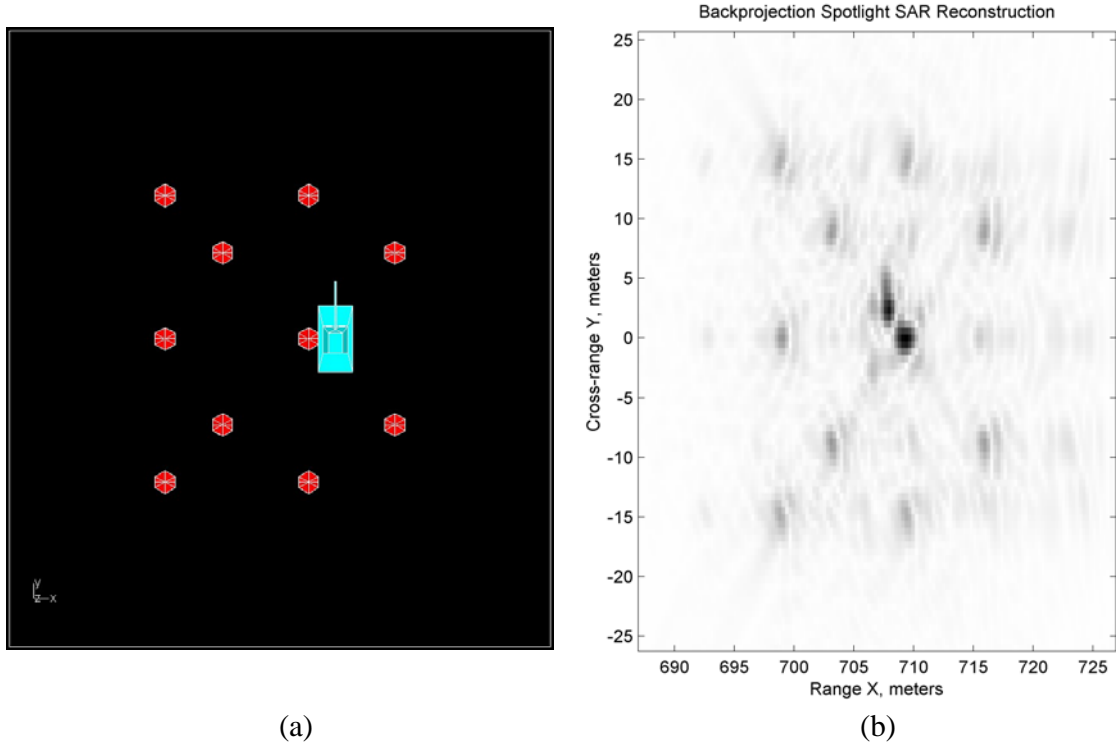


**Figure 32: (a) T80 tank and dielectric tree sparse forest WIPL geometry; (b) backprojection spotlight SAR reconstruction using superposition**

## 7.0 Scenes with moving targets

This section examines the feasibility of using WIPL to analyze target scenes with moving targets. When reconstructing SAR scenes with moving targets, the stationary scattering objects become the “clutter” and the desired signals are the moving targets [5]. This is a very difficult problem in terms of simulation. Since the target scene is changing, the impulse response for each individual aperture point is different, necessitating a complete simulation of the scene over the entire radar pulse bandwidth for each individual aperture point. Each aperture point sees the target scene differently, so the impulse response for the scene is different at each point (not just a change in the monostatic excitation direction for each individual aperture point). This increases the simulation time vastly. The total simulation time becomes that required for a single static scene times the number of aperture points. Since the simulation time is already becoming prohibitively large, this type of problem is intractable for the single processor version and likely even problematic for the parallel version.

To demonstrate the effect of moving targets in a stationary reconstruction, the very basic scene shown in Figure 33 will be discussed. The WIPL scene shown in Figure 33 consists of a stationary trihedral in the upper region and a moving trihedral in the lower region. The moving trihedral is moved with a constant velocity in the  $45^\circ$  direction. The velocity of the lower trihedral will be varied from moving very slowly to relatively fast. The SAR dimensions and aircraft velocity are indicated in Table 3.

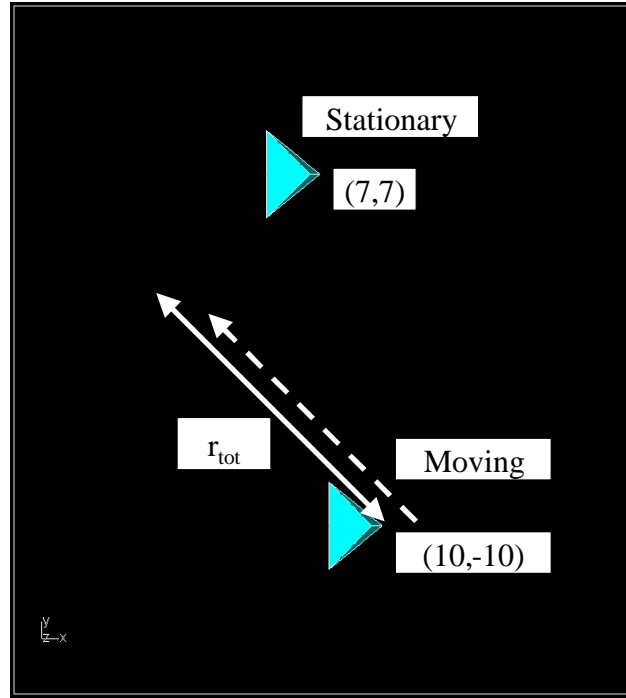


**Figure 33: Basic moving target example with a stationary and moving trihedral corner reflector.**

Parameter	Value
$X'$	500 m
$Z$	500 m
$X_{cc}$	707.1 m
$L$	182 m
<i>Total Aperture Length</i>	364 m
<i>Aircraft Velocity</i>	100 m/s
<i>Synthetic Aperture Time</i>	3.64 s

**Table 3: Moving target simulation parameter values.**

The reconstruction of the stationary scene is shown in Figure 34. In Figure 34a, the object is moving very slowly and appears almost stationary. Hence, it appears clearly in the reconstruction. In Figure 34b, the object's velocity is increasing and appears blurry in the reconstruction and its position is unclear. In Figure 34c, the object's velocity is such that it completely disappears in the reconstruction. While these

simulations confirm the ability of WIPL to analyze moving scenes correctly, the feasibility of using WIPL to analyze anything but trivially small target scenes is unlikely. Possible solutions to this difficulty are to employ the linear superposition approach to move the scattering objects around the scene. But again, this would only be valid if the scattering object had little interaction with the surrounding environment, and that is not the primary objective of this effort.

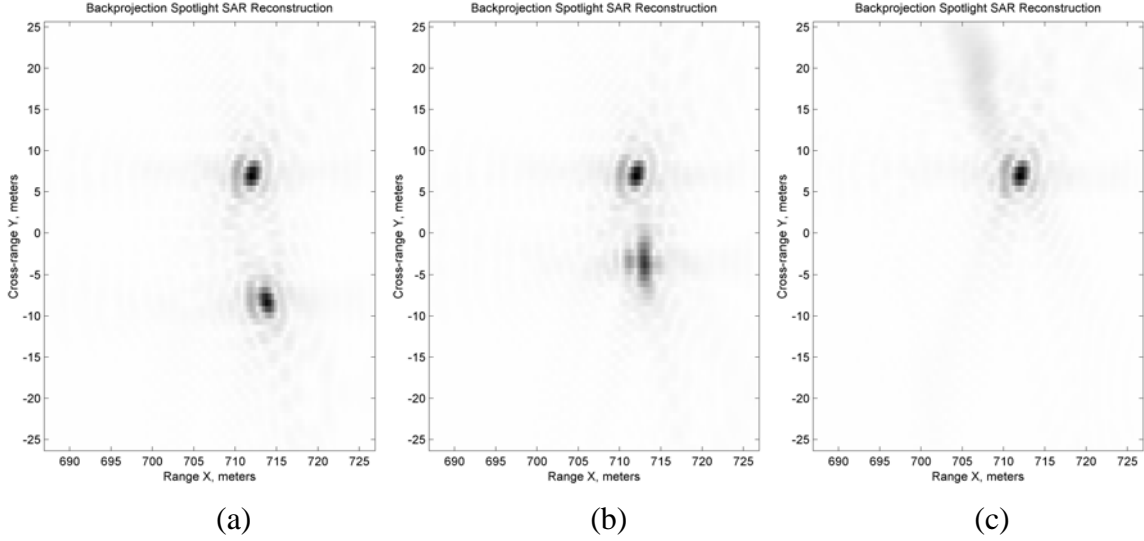


**Figure 34: Backprojection spotlight SAR reconstruction. (a)  $v=1.5\text{km/h}$ ; (b)  $v=5.0\text{km/h}$ ; (c)  $v=29.7\text{km/h}$ .**

## 8.0 Recommended WIPL-D Modifications

The development of this code, which uses WIPL-D generated data to produce SAR images of complex target scenes involving dielectrics and metals, has motivated some recommended modifications to future versions of WIPL-D to facilitate this and other code development. The most significant of these recommendations is the ability to arbitrarily define the monostatic incident wave excitation direction as can be done with bistatic simulations. Bistatic simulations can read an arbitrary incident excitation wave direction from the wave table while monostatic simulations must read the incident excitation wave direction from a  $\varphi_{start}$  to  $\varphi_{stop}$  and  $\theta_{start}$  to  $\theta_{stop}$  type enumeration table.

To understand why this is a problem, take the specific case of the synthetic aperture dimensions provided in Table 1. The angle  $\theta$  varies from  $\theta = 45^\circ$  at  $y = 0$  to  $\theta = 43.2^\circ$  at  $y = \pm L$ . Also, the angle  $\varphi$  is being varied from  $\varphi = 160^\circ$  at  $y = L$  to  $\varphi = 200^\circ$  at  $y = -L$ . To achieve the exact fields which correspond to these excitation wave directions,  $\theta$  would have to be varied from  $\theta = 43.2^\circ$  to  $\theta = 45^\circ$  while  $\varphi$  is simultaneously being varied from  $\varphi = 160^\circ$  and  $\varphi = 200^\circ$ . This would necessitate a field calculation for *each* of these  $\theta$  values over the entire synthetic aperture length from  $\varphi = 160^\circ$  to

$\varphi = 200^\circ$ . However, any specific aperture point has a unique  $(\varphi, \theta)$  for which the monostatic field calculation is required. Calculating the monostatic excitation over a range of  $\theta$  values in order to achieve a specific monostatic aperture point excitation translates into a significant amount of redundant field calculations, increasing the run time of simulations that are already appreciably large.

In order to temporarily circumvent this problem, the average value of  $\theta$  has been used across the aperture. Again, for the specific case of the synthetic aperture dimensions provided in Table 1,  $\theta$  varies from  $\theta = 43.2^\circ$  to  $\theta = 45^\circ$ . For the monostatic simulations,  $\theta$  has been set to the average value of  $\theta_{avg} = 44.1^\circ$  and  $\varphi$  has been set to sweep from  $\varphi = 160^\circ$  to  $\varphi = 200^\circ$  which is the synthetic aperture extent. Using the average value of  $\theta$  is essentially equivalent to introducing a motion error to the SAR signal. However, based upon the observed results where the targets appear at the correct range location and have the approximately correct dimension in the cross-range suggests that this error has a small effect upon the reconstructed images. When the synthetic aperture is moved closer to the STR, however, the angular error introduced by using the average  $\theta$  will become more significant since there is a larger variation in  $\theta$  for a given aperture length  $L$ . This is important since another way the resolution could be increased is by moving the synthetic aperture closer to STR (reducing  $X_{cc}$  in eqn. (3)). Also, in other possible applications such as spotlight mode GPR, the synthetic aperture will be appreciably close to the STR.

## 9.0 Review

This study demonstrated the usage of WIPL-D in the simulation of SAR scenes involving various types of targets, including combined metal/dielectric targets. The reconstructed targets are at the correct locations and have the correct dimensions. Also demonstrated were different aspects of radar behavior such as the effect of different polarizations and surface roughness on target reconstruction. Of particular interest are the preliminary results demonstrating FOPEN scene generation. The ability to predict target signatures under various conditions of concealment will be a significant application of this tool.

The capabilities of the single processor version of WIPL-D have been reached. The simulation of the simple FOPEN scene of a T80 tank and basic tree model in Figure 27 had more than 7000 unknowns (even using the reduced current expansion option) and took more than three weeks to complete on a single processor. The realistic FOPEN scene shown in Figure 28 simply cannot be analyzed with the single processor version over a frequency range that would be of interest in practice. This is because the run-time on a single processor would be prohibitive as well as the fact that the maximum number of unknowns (10,000) of the single processor version was reached.

The generation of realistic FOPEN scenes, such as that shown in Figure 28, over practical frequency ranges *will be* possible when WIPL-DP becomes available for use. The parallel version will simply extend the frequency range for the given scene. The results presented here demonstrate that this approach works and that WIPL-D can indeed be used for SAR imaging applications. The parallel version will build upon the framework developed here to enable the analysis of large FOPEN SAR scenes.

## 10.0 References

- [1] Ward, J., *Space-time adaptive processing for airborne radar*. 1994, MIT Lincoln Laboratory: Cambridge, MA.
- [2] Harrington, R.F., *Field Computation by Moment Methods*. 1982: Robert E. Kreiger Publishing Co.
- [3] Kolundzija, B.M., B.D. Popovic, *Entire-domain Galerkin method for analysis of metallic antennas and scatterers*. Proceedings of the IEE, Part H, 1992. 140(1):p. 1-10.
- [4] Kolundzija, B.M., B.D. Popovic, T.K. Sarkar, R.F. Harrington, *WIPL-D Professional Version*. 2000, OHRN Enterprises: Dewitt, NY.
- [5] Soumekh, B., *Synthetic Aperture Radar Signal Processing with MATLAB Algorithms*. 1999, New York: John Wiley.
- [6] Knott, E.F., Shaeffer, J.F., Tuley, M.T., *Radar Cross Section*. 1993, Artech House.
- [7] Carrara, W.G., Goodman, R.S., Majewski, R.M., *Spotlight synthetic aperture radar: signal processing algorithms*. 1995, Artech House.
- [8] Simcoe, M., Chen, E., Adve, R., Qureshi, F., Schneible, J., Wicks, M., *FOPEN Scene Generation Using Numerical Electromagnetic Analysis*. IEEE Conference on Radar, 2003. p. 362-369.